The Evolution of a Buoyant River Plume in Response to a Pulse of High Discharge from a Small Midlatitude River

EMILY LEMAGIE

Woods Hole Oceanographic Institution, Woods Hole, Massachusetts

JAMES LERCZAK

Oregon State University, Corvallis, Oregon

(Manuscript received 21 May 2019, in final form 25 April 2020)

ABSTRACT

A unique feature of small mountainous rivers is that discharge can be elevated by an order of magnitude during a large rain event. The impact of time-varying discharge on freshwater transport pathways and alongshore propagation rates in the coastal ocean is not well understood. A suite of simulations in an idealized coastal ocean domain using the Regional Ocean Modeling System (ROMS) with varying steady background discharge conditions (25–100 $m^3 s^{-1}$), pulse amplitude (200–800 $m^3 s^{-1}$), pulse duration (1–6 days), and steady downwelling-favorable winds (0–4 $m s^{-1}$) are compared to investigate the downstream freshwater transport along the coast (in the direction of Kelvin wave propagation) following a discharge pulse from the river. The nose of the pulse propagates rapidly alongshore at 0.04–0.32 $m s^{-1}$ (faster propagation corresponds with larger pulse volume and faster winds) transporting 13%–66% of the discharge. The remainder of the discharge volume initially accumulates in the bulge near the river mouth, with lower retention for longer pulse duration and stronger winds. Following the pulse, the bulge eddy disconnects from the river mouth and is advected downstream at 0–0.1 $m s^{-1}$, equal to the depth-averaged wind-driven ambient water velocity. As it transits alongshore, it sheds freshwater volume farther downstream and the alongshore freshwater transport stays elevated between the nose and the transient bulge eddy. The evolution of freshwater transport at a plume cross section can be described by the background discharge, the passage of the pulse nose, and a slow exponential return to background conditions.

1. Introduction

Discharge events from small mountainous rivers deliver significant concentrations of nutrients to the coastal ocean near Oregon (Sigleo and Frick 2007; Brown and Ozretich 2009) and globally contribute a significant fraction of the sediment and particulate carbon flux to the ocean (Milliman and Syvitski 1992; Vörösmarty et al. 2000). Unique features of these systems are the high degree of temporal intermittency in their discharge and the coherence in discharge between rivers. Understanding the transport pathways of the buoyant coastal plumes generated by pulses of discharge is important for understanding the fate of the materials supplied to the coastal ocean. Little scientific attention has been focused on intermittent river forcing on river plumes and coastal currents in general and from small mountainous rivers in particular.

The Oregon coast of the United States is an example of a midlatitude small mountainous river system (Burt and McAlister 1958; Hickey and Banas 2003; Wheatcroft et al. 2010). Rain from storm systems generates episodic pulses of freshwater in each river due to the small size and storage capacity of coastal range watersheds. Large storm events can elevate the river discharge more than an order of magnitude for short periods (Fig. 1a). Winter conditions off Oregon are characterized by predominantly downwelling-favorable winds and large river discharge (Huyer 1977; Huyer et al. 1979). These conditions can lead to along-shelf transport of buoyant water over long distances (tens to hundreds of kilometers) in a narrow coastal current (Mork 1981; Royer 1981).

Denotes content that is immediately available upon publication as open access.

Corresponding author: Emily Lemagie, elemagie@whoi.edu

DOI: 10.1175/JPO-D-19-0127.1

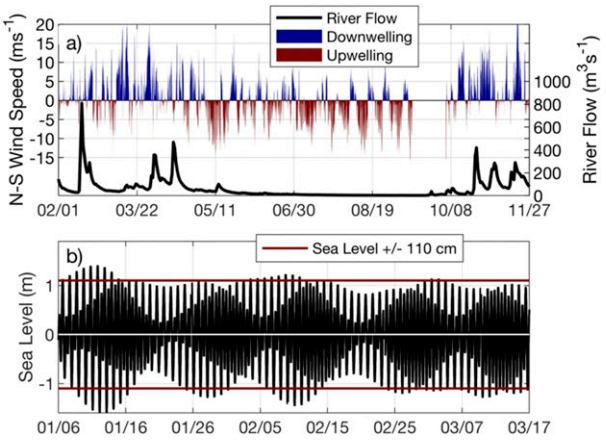

FIG. 1. (a) Northward wind speeds from the National Data Buoy Center station NWPO3 off of Newport, OR, and river discharge from the Alsea River provided by the U.S. Geological Survey and (b) 2 months of sea level measurements at the Waldport, OR, tide station 9434939 (https://tidesandcurrents.noaa.gov/) from the year 2010. Wind speeds are shaded to delineate upwelling- and downwelling-favorable periods. The winter season in Oregon is characterized by high discharge events and downwelling-favorable winds. The horizontal colored lines about the 2-month mean sea level mark the range of M_2 semidiurnal amplitude used to force the model.

With steady river discharge, the impact of wind and tidal currents on freshwater transport pathways has been investigated in laboratory, modeling, and observational studies. In the absence of wind or tidal forcing, Nof and Pichevin (2001) present an analytical theory on an f plane that predicts around 66% of the river outflow is retained near the mouth in a clockwise (in the Northern Hemisphere) rotating eddy. This region, where the recirculating flow is in gradient wind balance, is referred to as the bulge (e.g., Yankovsky and Chapman 1997). The plume from a river with a low Kelvin number, $K < 1$ (Garvine 1995; Avicola and Huq 2003), and Froude number, $F \geq 1$, at the river mouth is likely to form such a bulge (Fong and Geyer 2002; Avicola and Huq 2003), as observed for example near the Columbia River (Horner-Devine 2009; Horner-Devine et al. 2009). Downstream of the bulge, the remainder of the outflow propagates alongshore in a geostrophically balanced coastal current.

The fraction of the outflow that is retained in the bulge has been observed to correspond with the aspect ratio of the alongshore and across-shore geometry of the bulge and the angle with which the currents impinge on the coastline (Whitehead 1985). Onshore Ekman transport and alongshore wind-driven flows due to downwelling-favorable winds cause the bulge to narrow (in the across-shore direction) and increases the fraction of freshwater transported downstream (e.g., Choi and Wilkin 2007; Chant et al. 2008). Discharge oscillations at tidal frequencies do not have a significant impact on the bulge geometry or downstream transport (Yankovsky et al. 2001; Yuan et al. 2018), although in the case where shelf tidal currents are large, tides may increase downstream freshwater transport by narrowing the bulge (Chen 2014).

Elevated discharge lasting longer than a tidal period (days), has been observed to increase the size of the bulge (Yankovsky et al. 2001; Hunter et al. 2010) and alter the retention of water within the bulge (Yuan et al. 2018). Yankovsky et al. (2001) use a numerical model to examine the impact of periodic variations in outflow velocity and of a single pulse of elevated discharge with an increased density anomaly relative to the background outflow on the bulge structure. With a single pulse of discharge and an ambient alongshore current, the bulge grows and then is advected downstream after the pulse has ended. More recently in a laboratory experiment, Yuan et al. (2018) studied the impact of periodic discharge on the retention rate of freshwater volume in the bulge and the corresponding transport farther alongshore. In response to changing discharge, the bulge alternately became wider and more compressed alongshore, changing the angle with which the currents impinge on the coastline and thus the fraction of the freshwater transported downstream. The fraction of freshwater transported downstream was more sensitive to variations in the oscillation period than oscillation amplitude (Yuan et al. 2018). These experiments do not consider wind or tidal forcing and leave the pathways of freshwater transport following a pulse of high discharge under a range of forcing conditions, as well as the propagation speed of the freshwater transported farther alongshore yet unexplored.

Observations have shown that the alongshore propagation speed of the freshwater transported into the coastal current can similarly depend on the forcing conditions. For example, variations in river discharge have been found to be correlated with alongshore coastal current velocities in the Delaware coastal current and the Gulf of Maine with a lag between velocities in the buoyant coastal current and river discharge on the order of days to weeks (Münchow and Garvine 1993; Geyer et al. 2004). Lentz and Helfrich (2002) proposed a steady, linear theory to predict the propagation speed of a bottom-trapped coastal current depending on the density anomaly, depth, and bottom slope which was expanded by Lentz and Largier (2006) to include the impact of wind forcing. This predicted propagation speed depends on both the theoretical

propagation speed of a gravity driven current along a vertical wall,

$$c_w = (g'h)^{-1/2}, \tag{1}$$

and the nose propagation speed in the limit of a small bottom slope,

$$c_\alpha = \frac{\alpha g'}{f}, \tag{2}$$

where g' and h are the reduced gravity and maximum plume depth, respectively, and α is the constant shelf slope. In this theory, c_{pred} is given by

$$c_{\text{pred}} = v_{\text{amb}} + c_w\left(1 + \frac{c_w}{c_\alpha}\right)^{-1}. \tag{3}$$

The term v_{amb} is the tidally averaged (wind-driven) alongshore velocity of the ambient coastal ocean. The ratio $c_w c_\alpha^{-1} \sim W_\alpha W_w^{-1}$, where W_α and W_w are the width of the plume on- and offshore of the foot where the plume intersects the bottom, and can be used to estimate whether the plume is surface trapped or slope controlled (Lentz and Helfrich 2002).

Here we investigate the evolution of the buoyant plume following a pulse of elevated discharge from a small river in an idealized model domain which includes a river channel and periodic tidal forcing. The specific objectives of this paper are to 1) calculate the rate of alongshore freshwater volume transport following the discharge pulse; 2) examine the influence of the estuary and the bulge on freshwater transport farther alongshore; and 3) determine the impact of pulse duration, peak amplitude, steady background discharge and downwelling-favorable winds on the freshwater transport rates and distribution. This study is organized as follows. In section 2 the model domain and setup are described, which are based on conditions representative of discharge from a single river along the Oregon coast in wintertime. The Oregon coast is particularly well suited for this study because of the distributed small mountainous rivers whose discharge is highly variable on episodic time scales in wintertime. Oregon is also characterized by downwelling-favorable winds which can lead to transport of the plume long distances along the coast. In section 3 the evolution of the plume is described by examining tidally averaged fields from one experiment. Next, the impact of the pulse characteristics and downwelling-favorable wind speed on estuarine adjustment, bulge growth, the propagation speed of the nose, and the propagation and decay of the transient bulge eddy are described. A case without winds is described in section 3f because of the significant qualitative differences in the response relative to the cases with wind forcing.

2. Methods

a. Numerical model

In this study we investigate an idealized model of a small mountainous river discharging into a coastal ocean domain using the Regional Ocean Modeling System (ROMS; Haidvogel et al. 2000; Shchepetkin and McWilliams 2005). The archetype for the model configuration is a representative small mountainous river along the Oregon coast, such as the Alsea River (Fig. 1; Wheatcroft et al. 2010). The model coastal domain extends 300 km alongshore (the y direction) and 75 km in the cross-shore (x) direction on a Cartesian grid (Fig. 2b). A 125-km-long rectangular river channel is added at $y = 0$ km. The width and depth of this channel are constant, $w_r = 500$ m and $h_r = 5$ m, respectively. Along the coastal boundary is a 5 m wall with a free slip boundary condition. The shelf slope is $\alpha = 0.0039$ such that the shelf break is 50 km offshore at 200-m depth. After the shelf break the domain continues to deepen offshore with a slope of 0.053 until 65 km from the coast where it reaches an abyssal depth of 1000 m.

The model is highly resolved in both space and time. The cross-shore grid spacing is 50 m within the first 10 km of the coast, linearly telescoping to 5 km offshore. The alongshore spacing is 100 m around the river mouth from $y = -2$ to 8 km (within the smaller white box in Fig. 2b), resulting in 5 grid points across the 500-m-wide river channel. The y-grid resolution telescopes alongshore to 500 m at $y = -30$ and 100 km (i.e., within the larger white box in Fig. 2b) and to as wide as 5000 m near the boundaries. The grid is $421 \times 409 \times 25$, with vertical resolution focused near the surface (s-coordinate parameters used here are $V_{\text{stretching}} = 4$, $h_c = 30$ m, $\theta_s = 5$, $\theta_b = 0.6$). Within 10 km of the coast the vertical resolution is less than 1 m through the upper 5 m of the water column and less than 5 m throughout the water column. The baroclinic time step is 23 s with a barotropic time step that is 20 times faster.

Vertical mixing of momentum and tracers is parameterized by the k–ε version of the generic length scale (GLS) turbulence closure formulation (Umlauf and Burchard 2003) with the Galperin stability function (Galperin et al. 1988). The splines density Jacobian is applied for the pressure gradient algorithm (Shchepetkin and McWilliams 2005). The model uses parabolic splines reconstruction of vertical derivatives and the recursive, multidimensional positive definite advection transport

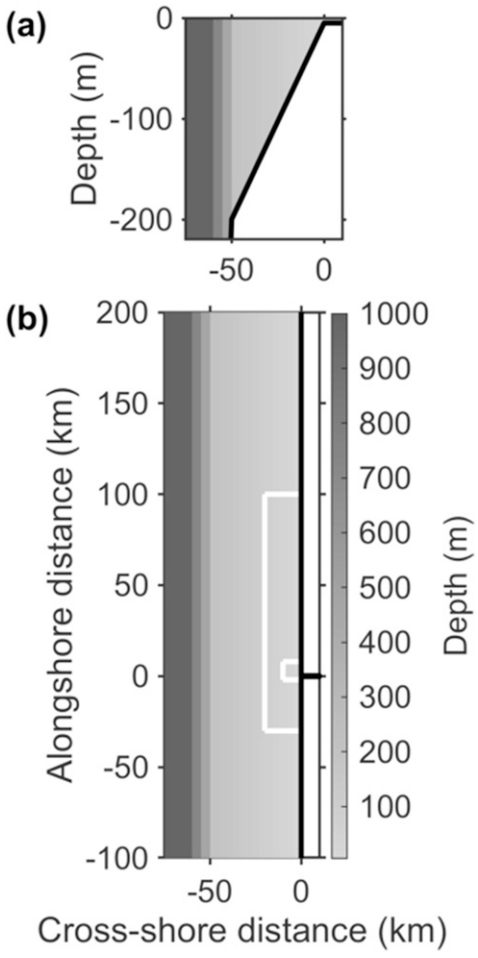

FIG. 2. Model domain and bathymetry shown with (a) a cross-shore cross section of the coast and (b) a plan view. The river channel, located at $y = 0$ km, is 5 m deep, 500 m wide, and 125 km long (full extent not shown). The coastal domain extends 75 km across shore and 300 km alongshore. Within the smaller white box (which extends 15 km into the river channel), horizontal grid resolution is 50 m in the cross-shore direction and 100 m alongshore. Inside of the larger white box in (b), horizontal grid resolution is less than 500 m. From this region toward the boundaries, resolution telescopes to a maximum of 5 km in both directions. The shelf slope is 0.0039 to 50 km offshore, the average Oregon slope. Beyond 50 km, the domain deepens with a slope of 0.053 to an abyssal depth of 1000 m; the full depth is not shown in (a).

algorithm (MPDATA) for horizontal tracer advection (Smolarkiewicz and Clark 1986). Three-dimensional momentum is advected by a third-order upstream bias scheme in the horizontal and a fourth-order centered difference scheme in the vertical direction (Shchepetkin and McWilliams 1998). A minimum background vertical diffusion coefficient for both momentum and tracers of $5 \times 10^{-6}\,\mathrm{m^2\,s^{-1}}$ is applied. There is no imposed horizontal tracer diffusivity or horizontal viscosity in the model equations. Bottom friction is parameterized by a quadratic drag law with a nondimensional drag coefficient of 3×10^{-3}.

Each model simulation is initialized in a quiescent state with no offshore stratification. The coastal domain has constant background salinity of $S_0 = 32$ psu ($\rho_0 = 1027\,\mathrm{kg\,m^{-3}}$). Between 16 and 22 km upriver there is an initial imposed linear horizontal salinity gradient from 32 to 0 psu. Temperature is fixed at 4°C and heat fluxes are not included in the model dynamics. A linear equation of state is specified. The Coriolis parameter is a constant, $f = 10^{-4}\,\mathrm{s^{-1}}$.

The freshwater inflow is representative of values that are typically observed in the Alsea River during the spring and fall or during a peak storm event (Fig. 1a). Freshwater inflow is introduced as a boundary condition evenly distributed over the grid at the head of the river with magnitudes of $Q_B = 25$, 50, 100, 200, 400, or $800\,\mathrm{m^3\,s^{-1}}$ (Table 1). Background discharge rates of 25, 50, and $100\,\mathrm{m^3\,s^{-1}}$ represent the relatively constant periods of discharge between storm events. Experiments EXP10–18, with steady discharges of $200–800\,\mathrm{m^3\,s^{-1}}$, are not representative of the range of realistic conditions for this system, but are included for comparison to the pulsed discharge experiments EXP1–9 (Table 1).

For simulations with winds, a spatially constant alongshore (downwelling-favorable) surface wind stress is applied. Figure 1a provides an example of upwelling and downwelling wind speeds along the Oregon coast. Wind speeds are strongly correlated; a single EOF mode of data from three stations that span over 375 km of the coastline captures over 90% of the variability. Although peak wind speeds reach over $20\,\mathrm{m\,s^{-1}}$, these peaks are not sustained over multiple days, so a maximum of $4\,\mathrm{m\,s^{-1}}$ steady winds is used. Surface wind stresses were calculated from wind speeds following Zeng et al. (2002).

Barotropic tides are imposed at the open boundary as a Kelvin wave at the M_2 frequency and a phase speed of $110\,\mathrm{m\,s^{-1}}$ alongshore, matching the propagation characteristics along the Oregon coast. Tides are ramped up over the first day of each model run. Only the M_2 tidal constituent is used to reduce the temporal variability in the forcing at subtidal time scales. For this study, tidal amplitudes of $A_{M2} = 110$ cm are used, representative of the mean tidal range of the mixed semidiurnal tides on the Oregon coast (Fig. 1b). The resulting alongshore tidal velocities have amplitudes of up to $0.075\,\mathrm{m\,s^{-1}}$. This is within the range of M_2 tidal velocities estimated off Oregon, but on the high end of that range (Barth and Wheeler 2005).

The Chapman condition (Chapman 1985) is applied for the free surface at all of the open ocean boundaries with the Flather condition (Flather 1976) at the offshore boundary that parallels the coastline for depth-averaged

TABLE 1. The full set of simulations with different combinations of river discharge pulse amplitude and duration. This first column lists the labels for each simulation. Columns 2–6 describe the forcing in each case, including the background discharge, pulse amplitude, pulse duration, resulting pulse volume, and downwelling-favorable wind speed, respectively. Columns 7–9 describe the plume in steady state before the pulse is applied, including the ratio of the coastal current width on- and offshore of the foot of the plume, the aspect ratio of the alongshore length L to the across-shore width W of the bulge, and the plume-average alongshore velocity. The last four columns report the exponential decay time scales at the river mouth, and $y = 40$ km as well as the freshwater volume in the nose of the pulse and the nose propagation speed.

	Q_B ($m\,s^{-1}$)	Q_P ($m\,s^{-1}$)	T_P (days)	V_P (km^3)	v_{wind} ($m\,s^{-1}$)	$W_\alpha W_w^{-1}$ (at $y = 40$)	L:W (bulge)	$\langle v_{31.9} \rangle$ ($m\,s^{-1}$)	$\tau_{x=0}$ (days)	$\tau_{y=40}$ (days)	$V_n V_P^{-1}$ (at $y = 40$)	c_n, c_s ($m\,s^{-1}$)
EXP1	25	200	3.1	3×10^{-2}	2	1.8 ± 0.9	1.9	0.1 ± 0.01	1.1	4.3	0.35	0.14
EXP2	25	400	3.1	6.4×10^{-2}	2	1.8 ± 0.9	1.9	0.1 ± 0.01	1	5.3	0.35	0.22
EXP3	25	800	3.1	1.3×10^{-1}	2	1.8 ± 0.9	1.9	0.1 ± 0.01	0.6	5.7	0.4	0.32
EXP4	25	400	1	2.1×10^{-2}	2	1.8 ± 0.9	1.9	0.1 ± 0.01	1	3.8	0.13	0.14
EXP5	25	400	6.2	1.3×10^{-1}	2	1.8 ± 0.9	1.9	0.1 ± 0.01	0.9	7.2	0.5	0.24
EXP6	50	400	3.1	6×10^{-2}	2	2.2 ± 0.6	2.6	0.11 ± 0.02	0.7	5.8	0.36	0.23
EXP7	100	400	3.1	5.1×10^{-2}	2	1.7 ± 0.1	1.2	0.11 ± 0.02	0.6	7.8	0.4	0.25
EXP8	25	400	3.1	6.4×10^{-2}	4	2.9 ± 0.4	2.3	0.13 ± 0.01	0.9	1.2	0.66	0.26
EXP9	25	400	3.1	6.4×10^{-2}	0	1.3 ± 0.3	—	—	0.9	—	0.13	0.04
EXP10	200	—	—	—	2	1 ± 0.1	—	—	—	—	—	0.14
EXP11	400	—	—	—	2	0.8 ± 0.1	—	—	—	—	—	0.22
EXP12	800	—	—	—	2	0.3 ± 0.01	—	—	—	—	—	0.28
EXP13	200	—	—	—	4	3.1 ± 0.2	—	—	—	—	—	0.14
EXP14	400	—	—	—	4	4 ± 0.7	—	—	—	—	—	0.2
EXP15	800	—	—	—	4	1.7 ± 0.1	—	—	—	—	—	0.28
EXP16	200	—	—	—	0	0.3 ± 0.02	—	—	—	—	—	—
EXP17	400	—	—	—	0	0.4 ± 0.02	—	—	—	—	—	—
EXP18	800	—	—	—	0	0.4 ± 0.1	—	—	—	—	—	—

boundary-normal velocity. At the open boundaries at maximum and minimum y, a no-gradient condition is applied to the two-dimensional normal velocity field. Tracer and three-dimensional momentum fields are treated using a standard Orlanski boundary condition (Orlanski 1976). For a more thorough explanation of these options for ROMS, see Marchesiello et al. (2001).

b. River discharge

Each pulsed experiment is run with steady background discharge Q_B and constant downwelling-favorable surface wind stress until reaching a steady state. Each simulation evolves until the tidally averaged alongshore freshwater volume transport asymptotes to Q_B. An estimate of steady state is determined using a running 3 tidal cycle (1.6 day) mean of freshwater transport at $y = 100$ km. This smoothed transport estimate reaches within 10% of Q_B after 42, 25, and 32 days for river flows of 25, 50, and 100 $m^3 s^{-1}$ with 2 $m s^{-1}$ winds, respectively, and after 37 days for a river flow of 25 $m^3 s^{-1}$ with 4 $m s^{-1}$ winds. Without downwelling-favorable winds, the freshwater transport does not reach a steady state. Instead, the bulge accumulates freshwater volume and expands over time, such that after 42 days it is qualitatively different from EXP1–8, and therefore difficult to make comparisons about the evolution of the plume in response to the discharge pulse. To make comparisons more direct, EXP9 is initialized with 2 $m s^{-1}$ winds until steady state is reached, after which winds are decreased to 0 (over 1 day) for the remainder of the simulation in order to examine the response of the plume to a discharge pulse in the absence of wind forcing. Here, $t = 0$ is defined as the last tidal period with steady discharge, before the pulse begins. For EXP9, this occurs 3 days after the winds were stopped.

After time $t = 0$ in each pulsed discharge experiment (EXP1–9, Table 1), the discharge pulse at the head of the river Q_R has a half-sinusoidal shape:

$$Q_R(t) = \begin{cases} Q_B, & t \le 0, \\ Q_B + (Q_P - Q_B)\sin(\pi T_P^{-1} t), & 0 < t \le T_P, \\ Q_B, & t > T_P. \end{cases} \tag{4}$$

where Q_P is the pulse amplitude and T_P is the pulse duration. The pulse volume V_P is the discharge volume above background levels.

For comparison, experiments without a discharge pulse, but with higher values of Q_B (equal to the peak discharges Q_P from the pulsed experiments) are also examined (EXP10–18, Table 1). These are run with the same initial conditions as the pulsed experiments.

c. Defining the plume

The plume boundary is defined by the $S_b = 31.9$ psu contour. This specific value of S_b is somewhat arbitrary; the intent is to capture a majority of the freshwater volume from the river source while excluding water near the plume boundary that is predominantly oceanic. All of the analyses presented depend on the definition used to delineate the plume boundary. This is true of any plume study as it is common across the literature to define the plume by an isohaline (e.g., Hetland 2005; Horner-Devine et al. 2009). The sensitivity of the results to this definition of a plume boundary are examined by comparing results using different values of S_b.

We define three regions of the plume separated by cross sections at the river mouth ($x = 0$ km) and at $y = 40$ km downstream (Fig. 3): the estuary (within the river channel); the region near the mouth (between the river mouth and $y = 40$ km) which contains the bulge; and farther alongshore ($y > 40$ km). The boundary $y = 40$ km is chosen because, for all of the simulations, the greater plume width and the accumulation of freshwater volume associated with the bulge is upstream of this location. The alongshore location of the bulge is estimated by its characteristic peak in tidally averaged cross-shore width and cross-sectional area.

d. Mouth Kelvin and Froude numbers

The mouth Kelvin and Froude numbers are calculated in order to assess whether bulge formation is likely. The Kelvin number is the ratio between the width of the river mouth and the internal Rossby deformation radius, $K = w_r f (g' h)^{-1/2}$ (e.g., Garvine 1995; Fong and Geyer 2002; Horner-Devine et al. 2015). The Kelvin number $\langle K_{31.9} \rangle$ at the river mouth is from 0.15 to 0.19 for EXP1–9 at $t = 0$ and ranges from 0.25 to 0.32 at the peak, varying due to changes in both plume density and depth. Angled brackets $\langle\rangle$ denote tidal averaging, which is computed between low water to low water. The subscript denotes the cross-sectional average of a field within the plume boundary; for example, $\phi_{31.9} = A_{31.9}^{-1} \int_{A_{31.9}} \phi \, dA$, where $A_{31.9}$ is the time-dependent cross-sectional area bounded by $S_b = 31.9$ psu. Cross sections along the coast are taken in the x–z plane and cross sections at the river mouth are taken in the y–z plane at $x = 0$ km.

The Froude number $\langle F_{31.9} \rangle$ is also calculated at the river mouth by the ratio of the outflow velocity at the mouth to the internal shallow water wave speed. The tidally averaged Froude number at the river mouth ranges from 1.2 to 1.5 at $t = 0$ for EXP1–8, and from 1.7 to 2.4 at the peak. For EXP9, in which the wind speeds decrease from 2 $m s^{-1}$ prior to the pulse, $\langle F_{31.9} \rangle$ is 0.9 at $t = 0$. Thus, bulge formation is likely at

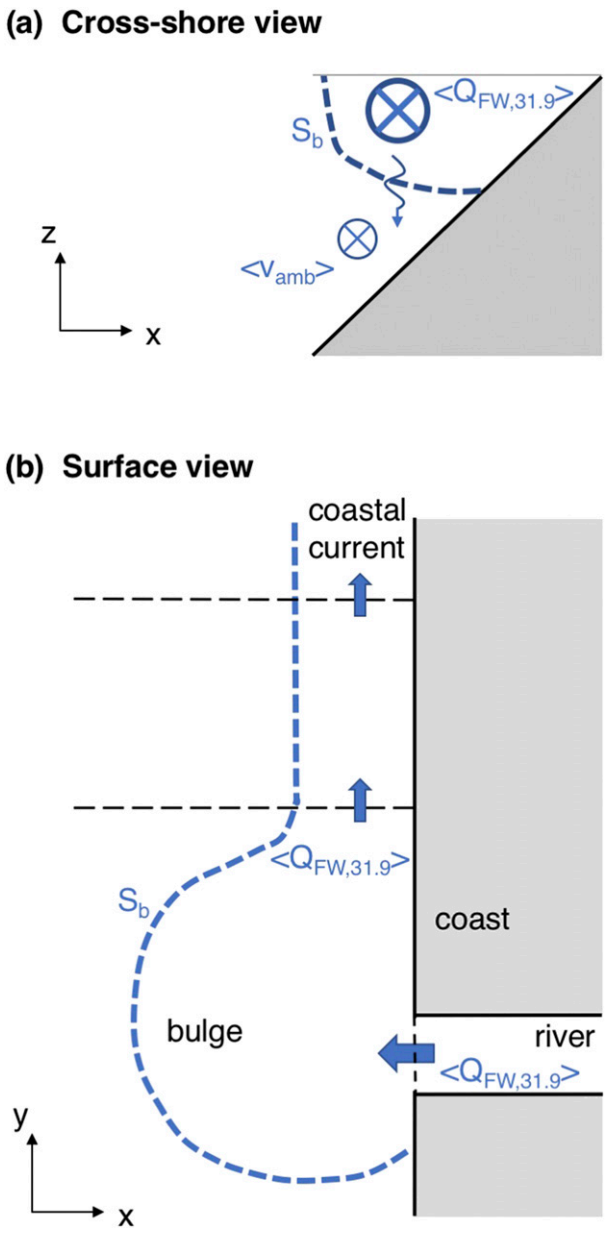

FIG. 3. Schematic of a plume showing the moving isohaline boundary S_b (blue lines) from (a) a cross-section view and (b) at the surface. Examples of the orientation of fixed vertical cross sections such as those at the river mouth and $y = 40$ km alongshore used to delineate the boundaries of the different regions within the plume (dashed black lines) are included in (b). Vector notation is used to demonstrate alongshore currents and freshwater transport within the 31.9-psu isohaline $\langle Q_{\mathrm{FW},31.9}\rangle$, and the squiggly arrow represents vertical mixing across the plume boundary.

all times in each simulation (Fong and Geyer 2002; Avicola and Huq 2003) and the conditions at the mouth of the estuary are consistent with high discharge from a small channel.

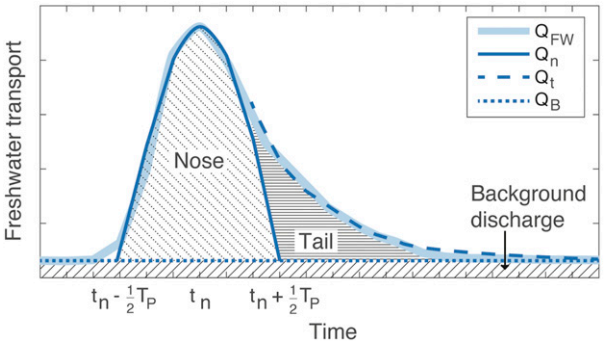

FIG. 4. Schematic of the downstream freshwater transport through a cross section of the plume, fit by three equations, as described in section 2e.

e. *Freshwater transport*

A focal point of this analysis is the tidally averaged freshwater transport $\langle Q_{\mathrm{FW},31.9}\rangle$ following a pulse of elevated discharge at the head of the river. The freshwater transport Q_{FW} is defined as the volume transport ($\mathrm{m^3\,s^{-1}}$) multiplied by the freshwater fraction, $F_{\mathrm{FW}} = (S_O - S)S_O^{-1}$, where S is the salinity.

We will show that the time evolution of the tidally averaged freshwater transport $\langle Q_{\mathrm{FW},31.9}\rangle$ at cross sections is fit well by three separate functions: 1) Q_B (before the arrival of the pulse); 2) a half-sinusoidal function with the same duration T_P as the discharge pulse, signifying the arrival of the pulse at a cross section (referred to as the nose of the pulse); and 3) an exponential tail during which $\langle Q_{\mathrm{FW},31.9}\rangle$ decreases to Q_B (Fig. 4). Thus, the nose of the pulse can be identified and the impact of the estuary and bulge in reducing the freshwater volume transport within the nose can be quantified. The freshwater transport of the nose is fit well at a cross section over time interval $-(1/2)T_P < t - t_n < (1/2)T_p$, by

$$Q_n(y, t) = (\langle Q_{\mathrm{FW},31.9}\rangle(t_n) - Q_B)\sin[\pi T_P^{-1}(t - t_n)], \qquad (5)$$

where $\langle Q_{\mathrm{FW},31.9}\rangle(t_n)$ is the maximum tidally averaged freshwater discharge at the cross section and t_n is the time of this maximum. The freshwater volume of the nose V_n is defined by the time integral of Q_n:

$$V_n(y) = \int_{t_n-(1/2)T_P}^{t_n+(1/2)T_P} Q_n(t)\,dt. \qquad (6)$$

After time t_n, there is a tail of elevated freshwater transport past each alongshore cross section, defined by $Q_t = \langle Q_{\mathrm{FW},31.9}\rangle - Q_n - Q_B$, which is fit by the exponential function

$$Q_t(y, t) = \beta \exp\left[\frac{-(t - t_n)}{\tau}\right]. \qquad (7)$$

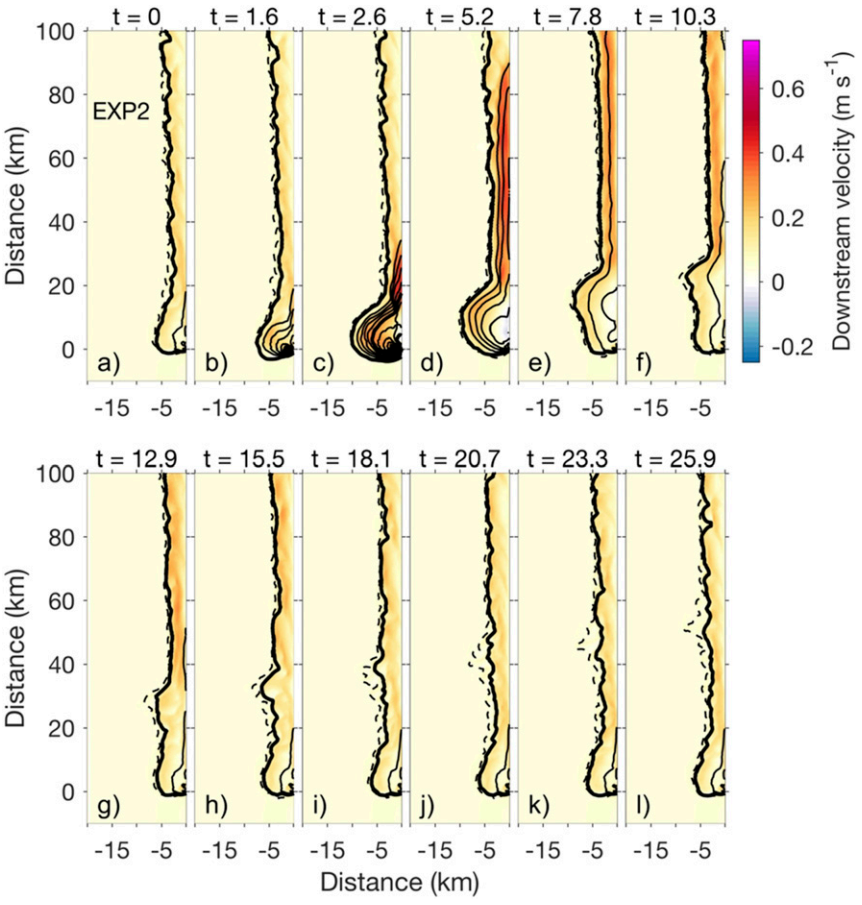

FIG. 5. Tidally averaged salinity and velocity profiles of the plume from simulation EXP2 at 12 times following the high discharge pulse. Alongshore velocities are shown in color overlaid by salinity contours. The outermost thick contour demarcates the 31.9-psu isohaline with thick and thin contour lines at 5- and 1-psu intervals, respectively. The thin dashed line is at 31.99 psu.

In Eq. (7), β is a fitting parameter and τ is an exponential decay time scale. This analysis focuses on comparisons of the freshwater volume in the nose and the tail at the river mouth and at $y = 40$ km (representative of the coastal current value).

The integral over the leading half of Q_n (from $t_n - T_P/2$ to t_n) accounts for over 98% of the integrated $\langle Q_{\mathrm{FW},31.9} \rangle$ over the same period for most simulations. The biggest deviation is in this fit for EXP4, which has a short pulse duration ($T_P = 1$ day) relative to the tidal period; using $T_P = 2$ days improves the analytical estimate.

3. Results

a. *The evolution of the plume following a pulse of river discharge*

This section describes the evolution of the plume in response to a discharge pulse. The tidally averaged surface fields (e.g., Fig. 5) and the plume-averaged freshwater transport, velocity, and salinity, as well as plume cross-sectional area and surface width are examined (e.g., Figs. 6a–d). The predominant characteristics of this response are qualitatively similar across all of the simulations with wind forcing (EXP1–8), so this section focuses on one example. EXP2 is chosen because it is forced with an intermediate peak discharge ($Q_P = 400\,\mathrm{m^3\,s^{-1}}$), and an intermediate pulse duration ($T_P = 6$ tidal cycles = 3.1 days). The largest deviations from this description occur in EXP9 discussed in more detail in section 3f.

The bulge near the river mouth initially grows and freshens following the pulse of river discharge and the shape becomes more round, steepening the angle with which the isohalines impinge on the coastline (Figs. 5b,c, 7d). At a cross section within the bulge the plume becomes fresher, especially near the surface, and a return flow develops which recirculates freshwater back into the bulge (Figs. 7b,d,f).

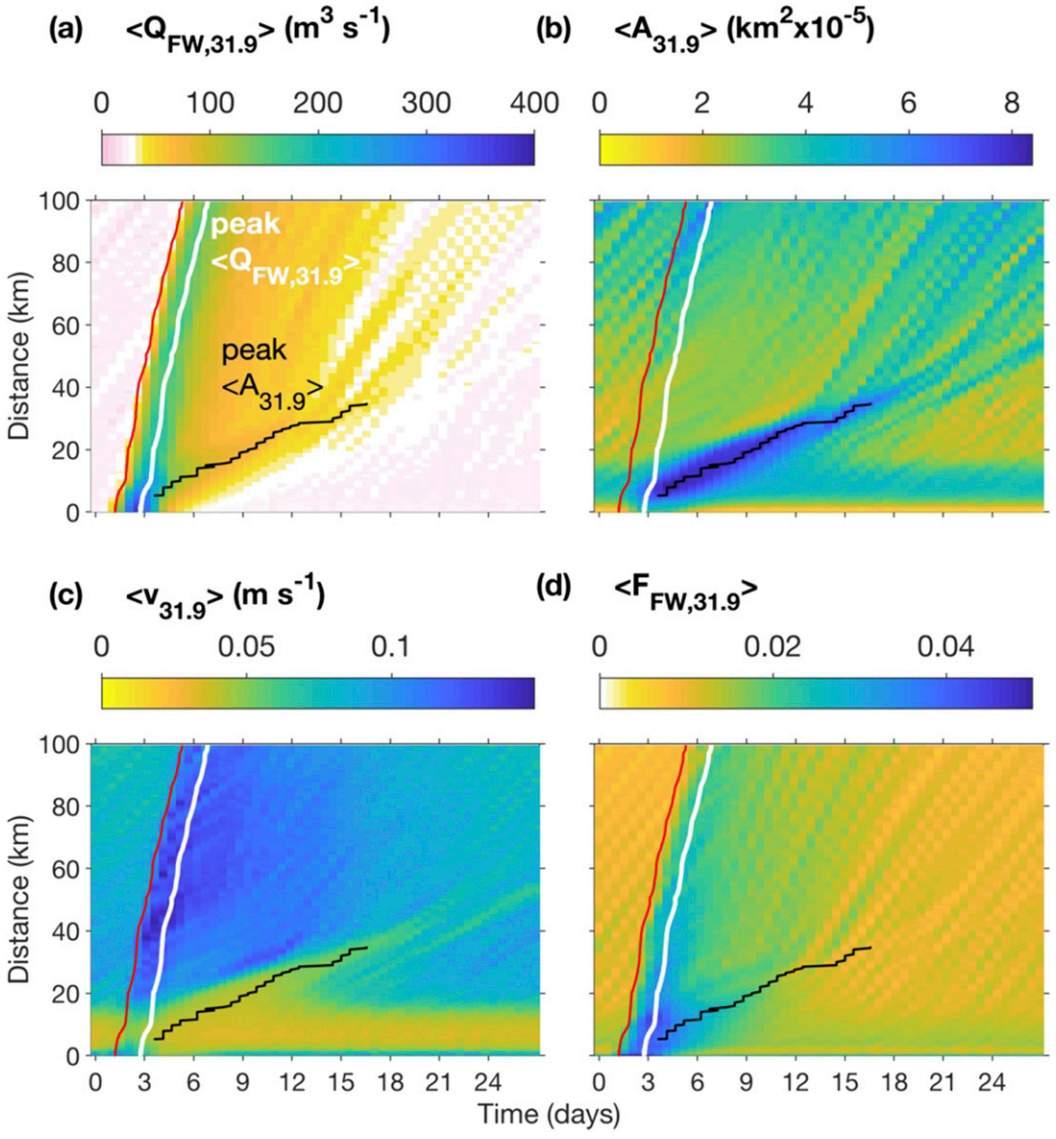

FIG. 6. (a) The tidally averaged freshwater transport within the 31.9-psu isohaline $\langle Q_{\mathrm{FW},31.9}\rangle$, (b) $\langle A_{\mathrm{FW},31.9}\rangle$, (c) $\langle v_{31.9}\rangle$, and (d) $\langle F_{\mathrm{FW},31.9}\rangle$ for EXP2 at cross sections alongshore following the pulse is plotted in color. The red line marks the downstream edge of the nose and the time when $\langle Q_{\mathrm{FW},31.9}\rangle$ past each downstream location has first increased above Q_B. The white and black lines trace the peaks in $\langle Q_{\mathrm{FW},31.9}\rangle$ (at time t_n) and $\langle A_{31.9}\rangle$, respectively, at each location alongshore.

A large fraction of the discharge pulse propagates rapidly alongshore in the nose (Figs. 5d, 6a, 8b). The nose is indicated by elevated freshwater transport, higher alongshore velocities and lower salinities (higher freshwater fractions), but no change in plume width or area (Fig. 6). When the nose passes $y = 40$ km, the plume near the surface and at the coast has a peak freshwater fraction more than 3 times greater than background conditions and there is a strong, vertically sheared alongshore jet reaching over 0.45 m s^{-1} at the surface (Fig. 7c). After the nose passes an alongshore location, freshwater fraction and transport remain elevated, with freshwater transport decaying exponentially to the background value (Figs. 8b, 6a,d).

Following the peak freshwater transport at the river mouth, the bulge begins to shift downstream. For example, by $t = 7.8$ days (Fig. 5e) the maximum width of the plume boundary is farther from the river mouth. By $t = 12.9$ days (Fig. 5g) there are two distinct peaks in the plume width along the coast, one near the river mouth and a larger peak nearly 30 km downstream referred to as the transient bulge eddy. The transient bulge is

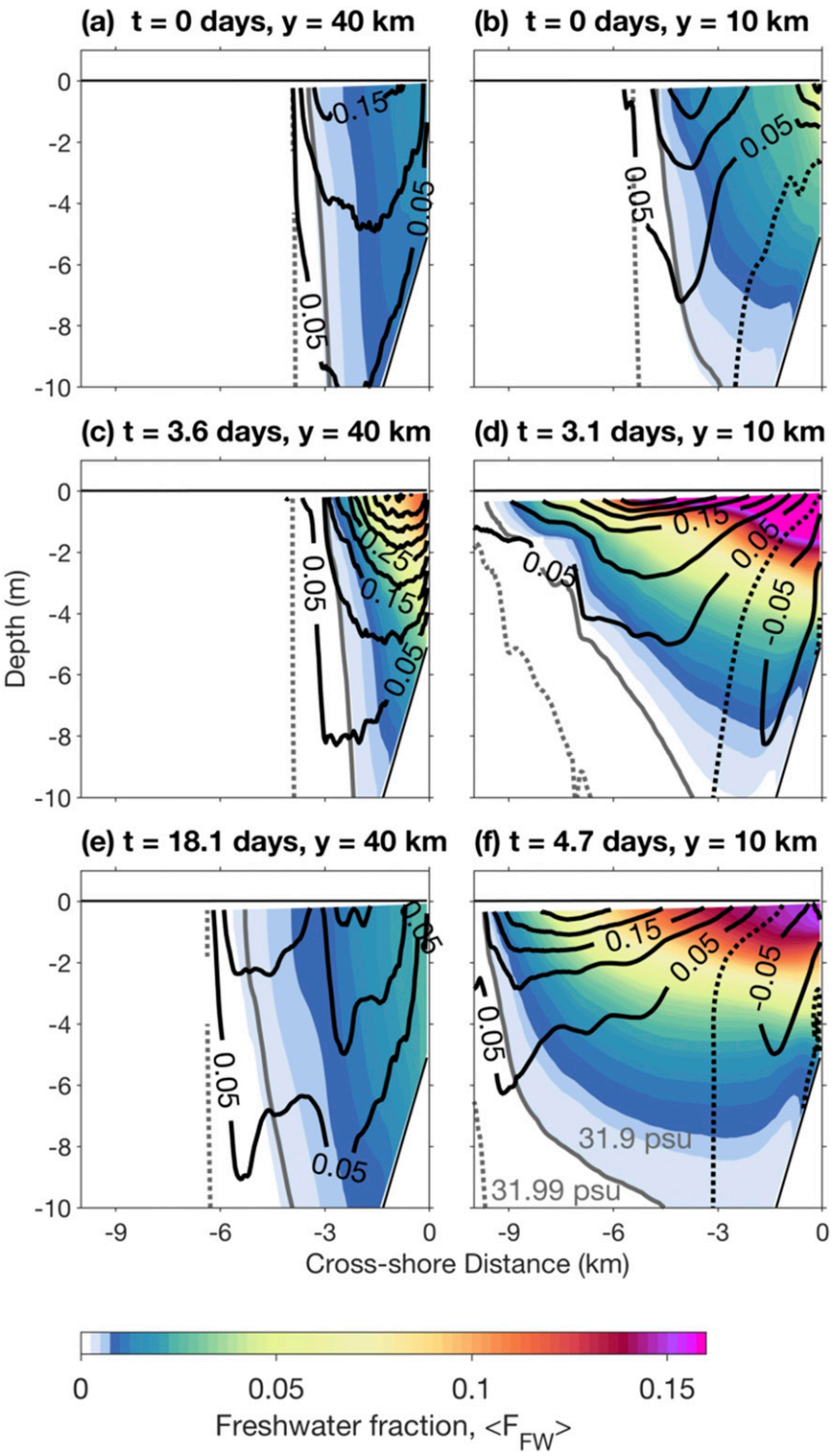

FIG. 7. Cross sections of tidally averaged fields from $y = 40$ km at (a) $t = 0$, (c) $t = 3.6$, and (e) $t = 18.1$ days as well as from $y = 10$ km at (b) $t = 0$, (d) $t = 3.1$, and (f) $t = 4.7$ days in EXP2. The freshwater fraction $\langle F_{FW} \rangle$ is shown in color. Black lines demarcate the 31.9-psu isohaline (solid line), and 31.99-psu (dashed line) contours. Alongshore velocities are contoured in black at 0.05 m s^{-1} intervals. The vertical structure at each cross section is shown at times corresponding with the steady-state condition in (a) and (b), the times of peak $\langle Q_{FW,31.9} \rangle$ in (c) and (d), and the times when the plume has the greatest area in (e) and (f).

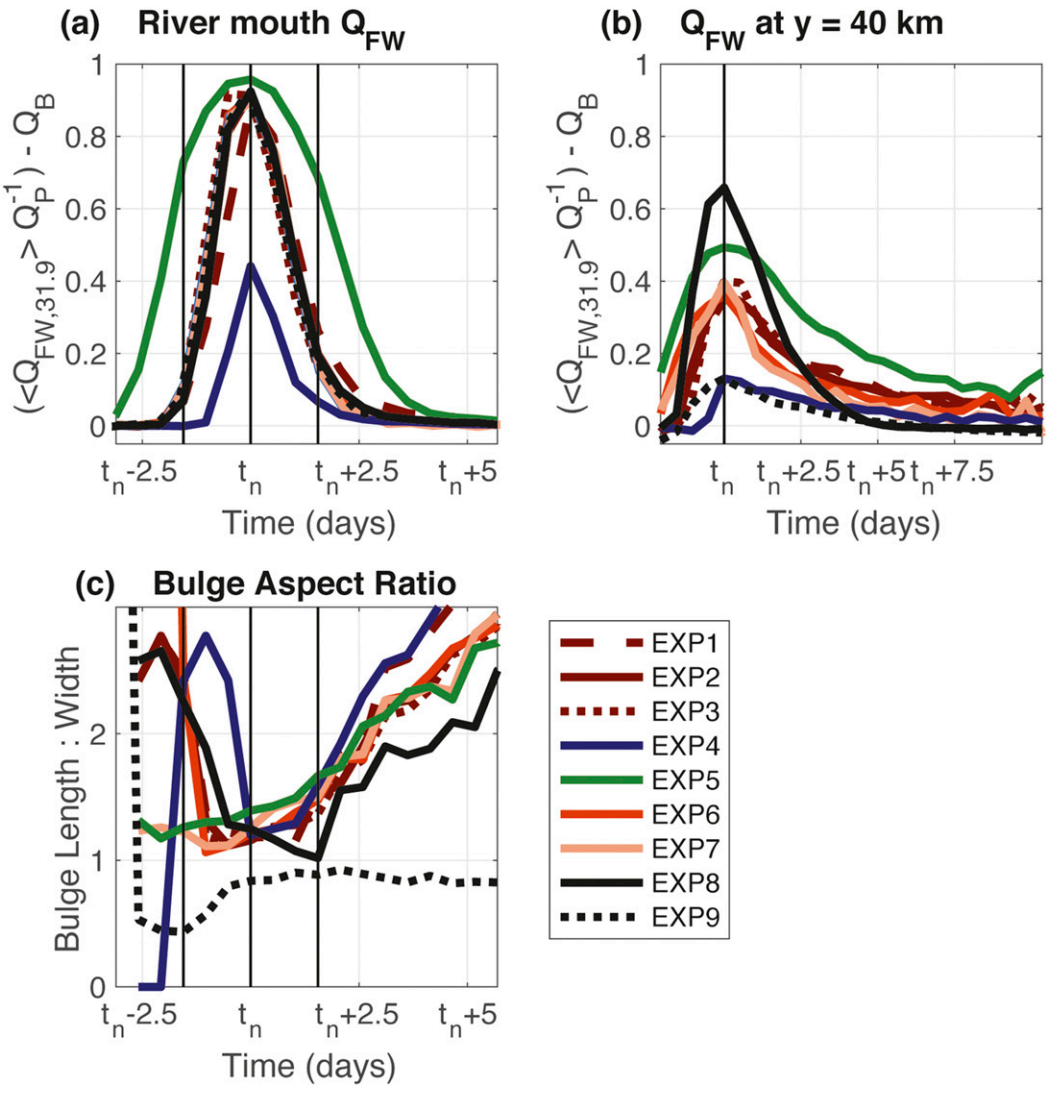

FIG. 8. (a) The freshwater transport within the 31.9-psu isohaline that defines the plume boundary at the river mouth over time, (b) at $y = 40$ km alongshore, and (c) the aspect ratio of the bulge alongshore length relative to its across-shore width. In (a) and (b) the background discharge Q_B is subtracted from each time series and the discharge is also normalized by Q_P in order to compare the symmetry of each run more directly. In (c) t_n is defined at the river mouth. Vertical black lines are plotted to emphasize the asymmetry of the discharge before and after the peak discharge occurs; there is a longer trailing edge following the peak in every experiment.

identified by a local maximum in $\langle A_{31.9} \rangle$ (Fig. 6b). This phenomenon has been observed in previous studies (e.g., Yankovsky et al. 2001), but its impact on freshwater transport is not well understood. The location of the peak in $\langle A_{31.9} \rangle$ corresponds with slightly elevated $\langle Q_{\mathrm{FW},31.9} \rangle$ (relative to Q_B; Fig. 6a) and $\langle F_{\mathrm{FW},31.9} \rangle$ (relative to background conditions at $t = 0$; Fig. 6d), but lower $\langle v_{31.9} \rangle$ (Fig. 6c). After the transient bulge eddy has passed an alongshore location, the conditions upstream of that point return to the steady state background conditions (Figs. 5g,l, 6). Over time the magnitude of the peak in $\langle A_{31.9} \rangle$ approaches the background value (Fig. 6b).

From this examination of the plume evolution following the discharge pulse, two distinct regions stand out: the nose, which propagates rapidly alongshore; and the bulge, which grows near the river mouth and propagates more slowly alongshore. The goal in the following sections is to further characterize the unique features, propagation rates, and associated alongshore freshwater volume transport within these regions.

b. *Estuarine adjustment*

The time evolution of freshwater transport can be described by the same 3 functions within the estuary as

along the coast (Figs. 4, 8a), despite the different dynamics that lead to this result. While at the head of the estuary, all of the freshwater volume is contained within the nose [Eqs. (4), (5)], at the estuary mouth some of the freshwater volume of the pulse is in the exponential tail, and $\langle Q_{\mathrm{FW},31.9} \rangle$ is not symmetric about time t_n (Fig. 8a). The exponential decay time scale, $\tau_{x=0}$ (Fig. 9a; Table 1), is quantified following Eq. (7). This exponential fit has an $R^2 \geq 0.95$ that is significant with 95% confidence. The tail is short ($\tau_{x=0} \sim 0.98 \pm 0.1$ days) and most of the pulse freshwater volume is within the nose (V_n accounts for 89%–95% of V_P) at the estuary mouth. The volume V_n is smallest for the smallest Q_P and greatest for the longest T_P. The tail is longest for the smallest Q_P, and shorter for higher Q_P and Q_B. These results are consistent with estuarine adjustment to changes in river discharge for which the adjustment time scale decreases with increasing discharge (Hetland and Geyer 2004; Lerczak et al. 2009). Although the timing and shape of the peak discharge at the mouth are likely to depend on characteristics in the estuary such as bathymetry, width, and length, as well as tidal conditions, which are all parameters beyond the scope of this study, this analysis suggests that estuarine adjustment modifies the pulse as it transits the estuary.

c. *The growth of the bulge*

The evolution of the shape of the bulge and the retention of freshwater volume following the discharge pulse are examined in order to explore the relationship between the angle of incidence with which the bulge circulation impinges on the coastline and the freshwater retention proposed by Yuan et al. (2018). First, the aspect ratio between the alongshore length L and across-shore width W of the bulge is determined. An alongshore length is estimated following Horner-Devine (2009), as the distance between the maximum tidally averaged onshore and offshore velocities in the top layer. The across-shore scale is estimated as the maximum tidally averaged offshore extent of S_b in the top layer.

The length-to-width aspect ratio L:W decreases to a minimum near the time of peak freshwater transport at the river mouth t_n and then continues to increase over time (Fig. 8c). After the occurrence of the minimum length-to-width aspect ratio, the maximum offshore velocity remains near the river mouth, while the maximum onshore velocity propagates alongshore with the transient bulge. Thus, the length scale is only representative of the core of a single bulge shortly following t_n at the river mouth. The exception to this pattern is EXP9, without wind forcing, where the aspect ratio responds to the decrease in winds from 2 to 0 m s^{-1} and does not exhibit a clear response to the discharge pulse.

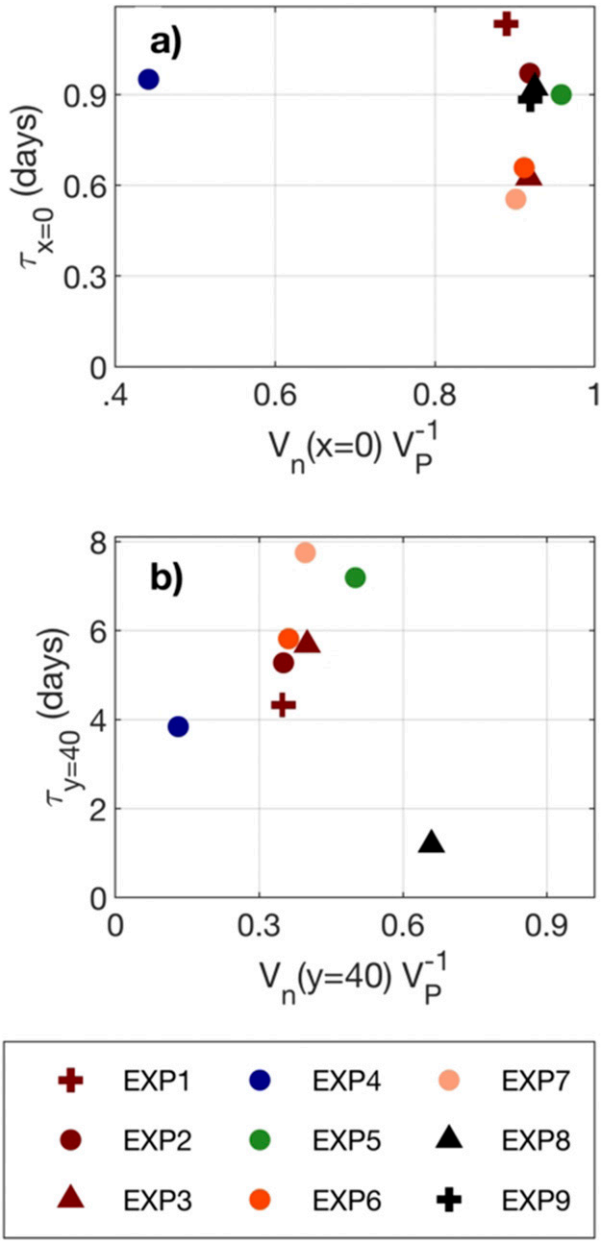

FIG. 9. The exponential decay time scale associated with the tail of elevated freshwater transport (a) behind the nose at the river mouth and (b) at $y = 40$ km relative to the fraction of the pulse volume contained within the nose at the corresponding cross section. Note the different axes scales.

For EXP1–8, the timing of the minimum aspect ratio of the bulge geometry was determined by a parabolic fit to the tidally averaged time series of L:W (e.g., Fig. 8c) within ±1 day of the minimum value.

The freshwater volume within the nose of the pulse V_n remains roughly constant beyond the bulge (i.e., for $y > 40$ km; e.g., Fig. 10). An estimate of the linear slope of V_n between $y = 40$ and 100 km indicates the

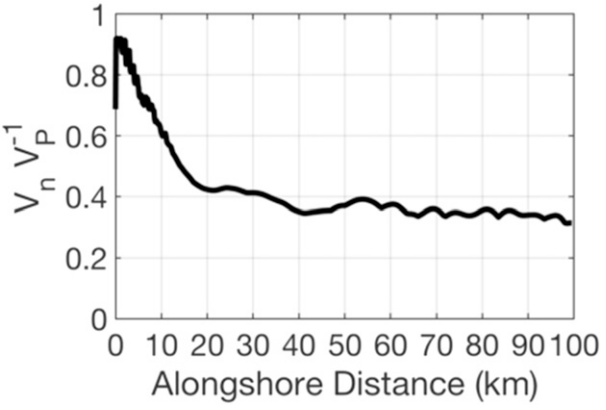

FIG. 10. The freshwater volume within the nose of the pulse as the nose propagates alongshore, normalized by the volume of the pulse at the head of the river V_P from EXP2.

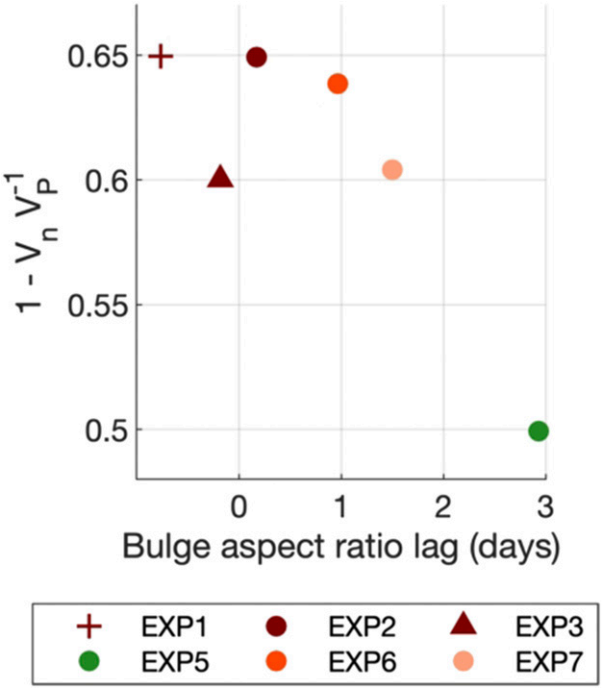

FIG. 11. The lag in the timing of the peak freshwater discharge at the river mouth following the minimum alongshore length to across-shore width aspect ratio of the bulge L:W compared to the percentage of the freshwater volume of the pulse that is transported past $y = 40$ km in the nose for selected experiments.

freshwater volume associated with the propagating nose decreases by ≤12% of V_P per 100 km for each pulsed discharge simulation. V_n at $y = 40$ km is 13%–66% of the discharge pulse (Table 1). The fraction of the pulse volume advected in the nose beyond $y = 40$ km is strongly dependent on wind and pulse duration, with more alongshore transport associated with stronger downwelling-favorable winds and a longer pulse. There is a weak dependence on Q_P and Q_B, with greater alongshore transport associated with greater peak and background discharges.

The significant decrease in the nose freshwater volume between the river mouth ($V_n \geq 89\%$ of V_P) and $y = 40$ km ($V_n \sim 13\%$–66% of V_P; Table 1, Figs. 8a,b) is due to the bifurcation of the circulation around the bulge when it impinges on the coastline, causing a percentage of freshwater volume from the nose to recirculate and accumulate near the river mouth (e.g., Whitehead 1985; Avicola and Huq 2003; Yuan et al. 2018).

The percentage of the pulse volume that is initially retained within the bulge is estimated as the pulse volume that is not transported downstream in the nose. The loss of freshwater volume across the plume boundary (S_b) due to vertical mixing near the river mouth—which is often a region of relatively high mixing rate (e.g., MacDonald and Geyer 2004; Hetland 2005; McCabe et al. 2008; Kilcher et al. 2012)—is small relative to the accumulation of freshwater within the bulge. The loss of freshwater volume across S_b is negligible within the river and past $y = 40$ km downstream. The mixing of freshwater volume across the plume boundary near the river ($y < 40$ km) is also small, but not negligible. Integrated over 10 days following the pulse, this accounts for less than 6% of V_P for all of the simulations with downwelling-favorable winds, and less than 12% of V_P for EXP9. If S_b is decreased, the relative importance of mixing correspondingly increases; for example, in EXP2 the mixing increases from 6% to 8% of V_P for S_b defined as 31.9 and 31.85 psu, respectively (a 50% decrease in freshwater fraction). At some threshold of S_b (for EXP2, 27.8 psu), the contribution of mixing near the river ($y < 40$ km) approaches 100%. However, for $S_b = 31.9$ psu, freshwater volume loss to the ambient ocean is not of first order importance in the budget of freshwater volume associated with the discharge pulse and the decrease in V_n between the river mouth and $y = 40$ km is primarily due to accumulation within the bulge.

More of the pulse freshwater volume is initially retained within the bulge when the timing of the minimum L:W aspect ratio of the bulge is closest to the timing of the peak freshwater discharge at the river mouth (for the experiments with 2 m s^{-1} winds; Fig. 11). The minimum bulge aspect ratio indicates the timing when the highest percentage of freshwater will be recirculated into the bulge; when this is coincident with the peak discharge, then the net retention over the duration of the pulse is maximized. In EXP5, with the longest pulse duration, the bulge aspect ratio reaches a minimum 1.5 days before the peak freshwater transport at the river mouth, and only 50% of the pulse volume is initially retained within the recirculating bulge.

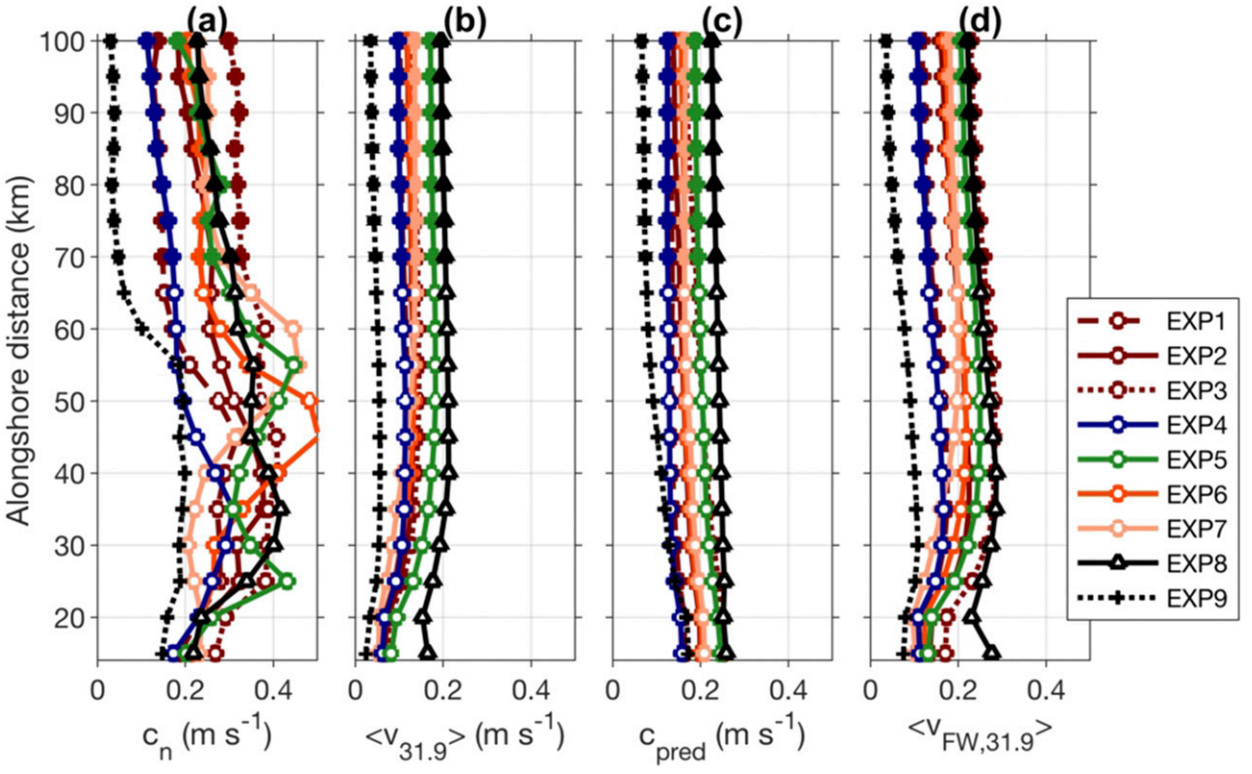

FIG. 12. (a) The tidally averaged propagation speed of freshwater transport, (b) tidally and area-averaged alongshore velocity, (c) theoretically predicted propagation speed, and (d) freshwater fraction weighted tidally and area-averaged alongshore velocity within the 31.9-psu isohaline at t_n, following the nose of the discharge pulse at 5-km increments alongshore for EXP1–9. Each point shown with a symbol represents the mean value of the field within ±15 km alongshore.

In EXP1–3, 5, and 6, the lag is less than 1 day and around 55%–60% of the pulse volume is initially retained in the recirculating bulge. This is consistent with the laboratory results of Yuan et al. (2018).

EXP4 was excluded from this comparison because the shorter duration pulse relative to the tidal-averaging interval leads to a less robust estimate of V_n. EXP8 and EXP9 are excluded because they have different wind forcing. Without winds, the bulge aspect ratio does not reach a minimum associated with the pulse. With stronger winds, the minimum L:W occurs after the transient bulge eddy may have already begun propagating downstream such that the method for estimating the alongshore length scale of the bulge is no longer valid.

d. *Fast alongshore propagation and velocities in the nose*

The alongshore propagation speed of the nose of the pulse c_n is determined by tracking the local peak in $\langle Q_{\mathrm{FW},31.9}\rangle$ alongshore (e.g., by the slope of the white line in Fig. 6a). This method is not sensitive to S_b; comparing c_n in EXP2 for different values of S_b between 31.85 and 31.91 psu does not change the result. In all of the simulations, c_n is variable and elevated for $y < 65$ km and settles to a more constant value by $y \approx 70$ km. Near the river mouth, and in the region of the bulge, ageostrophic, nonlinear, and nonsteady dynamics can be important relative to the coastal current farther alongshore (e.g., Horner-Devine et al. 2015). In an effort to compare the nose velocities and propagation to steady coastal current theory, a far-field mean value of c_n for distances between $y = 70$ and 100 km is reported as a representative nose propagation speed for EXP1–9 (Table 1 and Fig. 12a, filled symbols). Due to the relatively higher values of c_n for $y < 70$ km, this far-field mean value is less than the cumulative propagation speed of the pulse over the first 100 km of coastline by around 10%–50%, but the relative propagation speeds between simulations are the same.

The propagation speed of the nose is strongly dependent on the pulse volume and the presence of downwelling-favorable winds. For example, c_n more than doubles for $Q_P = 800\,\mathrm{m^3\,s^{-1}}$ compared to $Q_P = 200\,\mathrm{m^3\,s^{-1}}$ (Table 1). The speed c_n also strongly depends on T_P, with faster propagation speeds for longer

pulse duration. The nose propagates very slowly without wind forcing, but there is only a slight increase in c_n between 2 and 4 m s^{-1} winds that is less than the respective increase in v_{amb}. There is also a slight increase in nose speed with increasing Q_B.

For a given wind speed, the nose propagation speed is faster than or equal to the propagation speed under steady discharge c_s (Table 1). The term c_s is defined by tracking the downstream extent of the tidally averaged plume boundary S_b starting from initial conditions with a uniform coastal ocean salinity of S_0. In EXP10–15, which have downwelling-favorable winds, c_s reaches a constant value over time. Without winds c_s decreases over time and there is no representative propagation speed; experiments EXP16–18 are excluded from this comparison.

The influence of shear and stratification on the nose propagation speed are explored by comparing c_n to the plume-averaged alongshore velocity $\langle v_{31.9}\rangle(t_n)$ at the time t_n when the nose passes an alongshore location. A freshwater-weighted and area-averaged velocity $\langle v_{FW,31.9}\rangle(t_n)$ is also compared (Fig. 12d). The velocities $\langle v_{31.9}\rangle(t_n)$ and $\langle v_{FW,31.9}\rangle(t_n)$ do not exhibit the same degree of alongshore variability for $y \leq 70$ km as c_n (e.g., Figs. 12a,b,d). The speed c_n is also faster than $\langle v_{31.9}\rangle(t_n)$ in each experiment, indicating that shear and stratification within the plume are important, with faster velocities coincident with fresher water. This can be observed qualitatively by comparing the contours of freshwater fraction $\langle F_{FW}\rangle$ and alongshore velocities (Fig. 7c). The velocity $\langle v_{FW,31.9}\rangle(t_n)$ is faster than $\langle v_{31.9}\rangle(t_n)$, but slower than c_n; while faster velocities tend to be collocated with higher freshwater fraction water within the nose, these two fields do not perfectly coincide (Figs. 12, 7c). However, c_n is more strongly correlated with $\langle v_{FW,31.9}\rangle(t_n)$ than $\langle v_{31.9}\rangle(t_n)$ (Figs. 13a,b).

The dynamics controlling nose propagation speed are further explored by comparing the observed plume-averaged velocity and nose propagation speed to linear plume theory. The plume-averaged propagation speed of the nose c_{pred} is predicted following Eq. (3). The reduced gravity g' and plume depth h are calculated using $\langle F_{FW,31.9}\rangle(t_n)$ and $\langle h_{31.9}\rangle(t_n)$, respectively. Here, $W_\alpha W_w^{-1}$ ($\sim c_w c_\alpha^{-1}$) is $\mathcal{O}(1)$ for all of the pulsed simulations beyond $y = 40$ km (Table 1), and does not change appreciably with the passage of the nose. This indicates that interactions with the bottom result in a slower propagation speed than would be predicted for a surface-trapped plume. Equation (3) estimates the plume-averaged velocity in the nose $\langle v_{31.9}\rangle(t_n)$, which under steady and alongshore-uniform conditions for a well-mixed plume is equivalent to the nose propagation speed c_n. Some of the inherent assumptions that go into Eq. (3) are not met by this study, such as assuming the plume outside of the bulge has adjusted to a geostrophically balanced steady-state condition with little alongshore variability and assuming a constant bottom slope (while α is constant, the vertical coastal wall is on the order of half of the plume depth). The velocity $\langle v_{31.9}\rangle(t_n)$ converges to $c_{pred}(t_n)$ as the nose propagates alongshore toward $y = 70$ km (Figs. 12b,c, 13d). For y between 70 and 100 km, $\langle v_{31.9}\rangle(t_n)$ and c_{pred} are strongly correlated. This is likely due to using tidally averaged and plume area-averaged fields to compute c_{pred}, which effectively neglects stratification and shear within the plume. The speed c_n is not as well correlated with c_{pred} (Figs. 13c,d). However, the correlation between c_n and c_{pred} is statistically significant (Fig. 13c), which implies that c_n depends on g' (which is proportional to $\langle F_{FW,31.9}\rangle$), $\langle h_{31.9}\rangle$, and wind speed. Between $y = 70$ to 100 km, c_n and $\langle F_{FW,31.9}\rangle(t_n)$ are significantly correlated ($R^2 = 0.69$) as are c_n and v_{amb} ($R^2 = 0.27$). The plume depth $\langle h_{31.9}\rangle(t_n)$ is roughly consistent for y between 70 and 100 km. Thus, the density anomaly in the nose and ambient wind-driven velocities contribute to the variability of the nose propagation speed c_n between simulations.

e. *Advection and decay of the transient bulge*

The bulge initially accumulates a significant percentage of the pulse freshwater volume V_P. After the nose passes, the transient bulge sheds this freshwater volume at an exponential rate and the freshwater transport between the nose and the transient bulge approaches Q_B (Fig. 8b). The time scale $\tau_{y=40}$ (Fig. 9b; Table 1) is calculated by fitting the freshwater transport in the tail of the pulse at $y = 40$ km to an exponential function [Eq. (7)]. This function describes the tail of freshwater transport with R^2 values from 0.85 to 0.99, except in EXP7 where $R^2 = 0.45$, and EXP9 which is excluded from this analysis because with no winds the bulge continues to accumulate freshwater volume over time. The time scale $\tau_{y=40}$ has a strong dependence on wind speed; faster downwelling-favorable winds lead to a more rapid alongshore transport of freshwater volume (Table 1). The time scale $\tau_{y=40}$ is also strongly dependent on pulse duration; $\tau_{y=40}$ is longer with longer T_P. It is also slightly longer with greater background and peak discharge, Q_B and Q_P. Except in the case with 4 m s^{-1} winds, $\tau_{y=40}$ can be more than 2 times greater than T_P.

In the pulsed simulations with winds (EXP1–8), the transient bulge eddy moves downstream after the discharge pulse subsides. Similar to the method for estimating c_n, this alongshore propagation speed of the transient bulge c_{tb} is estimated by the slope of the line that traces the local maximum in $\langle A_{31.9}\rangle$ (e.g., Fig. 6b). The speed c_{tb} is almost entirely dependent on wind speed (Fig. 14). For experiments with 2 m s^{-1} downwelling-favorable winds (EXP1–7) c_{tb} is between 0.028 and 0.032 m s^{-1}, which is similar to the depth-averaged, tidally averaged alongshore velocity of the ambient coastal ocean v_{amb}.

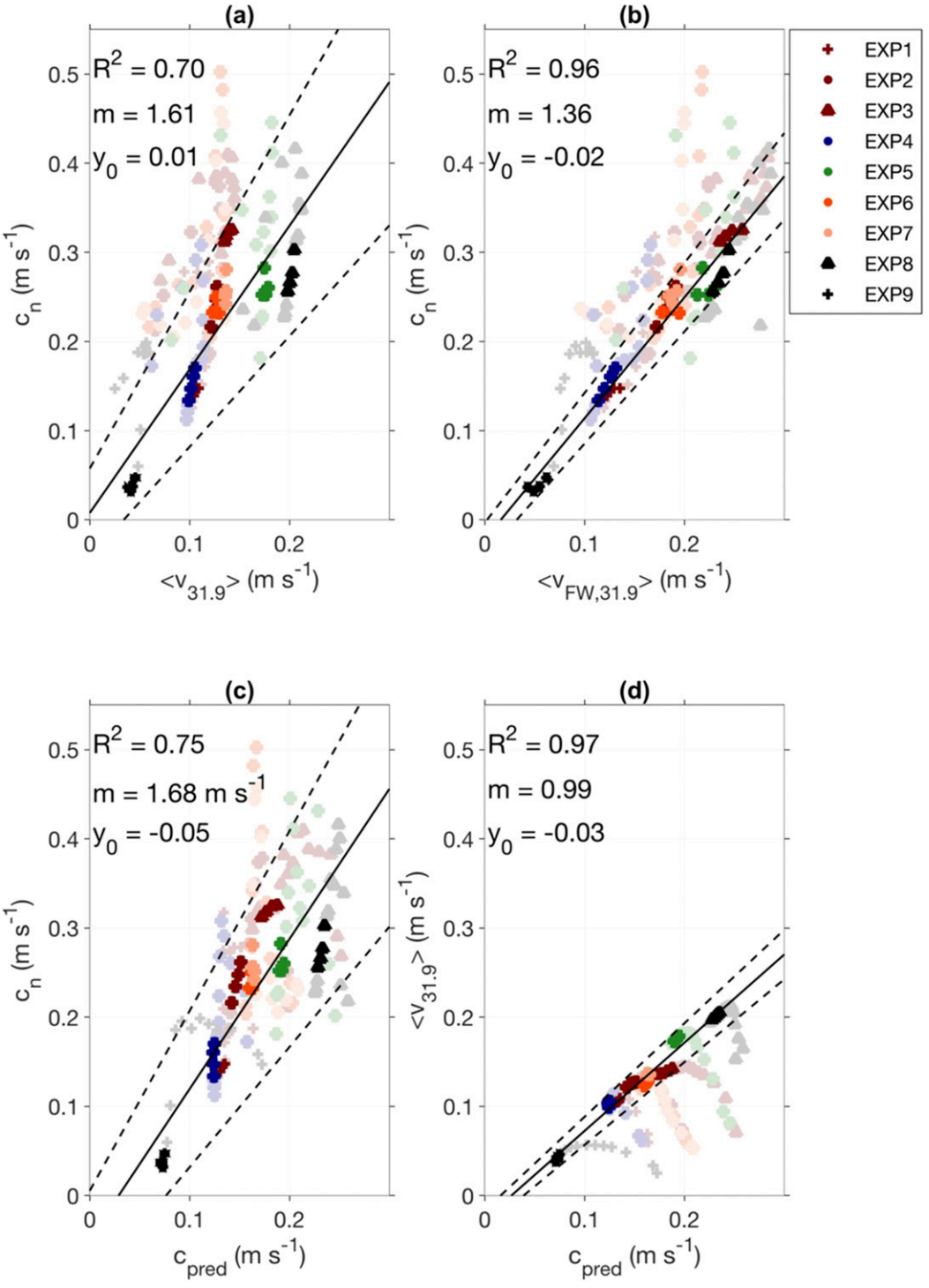

FIG. 13. Comparisons of (a) $\langle v_{31.9} \rangle$ and c_n, $R^2 = 0.7$, slope $m = 1.61$, and intercept $y_0 = -0.01$; (b) $\langle v_{\mathrm{FW},31.9} \rangle$ and c_n, $R^2 = 0.96$, $m = 1.36$, and $y_0 = -0.02$; (c) c_{pred} and c_n, $R^2 = 0.75$, $m = 1.68$, and $y_0 = -0.05$; and (d) c_{pred} and $\langle v_{31.9} \rangle$, $R^2 = 0.97$, $m = 0.99$, and $y_0 = -0.03$. Darker (lighter) shaded symbols correspond to y greater than (less than) 70 km. Solid black lines show the linear regression fit to the darker shaded symbols, with dashed lines showing the 95% confidence intervals. The regression R^2, slope m, and y intercept y_0 (m s^{-1}) are labeled in each panel where the regression is significant with 95% confidence.

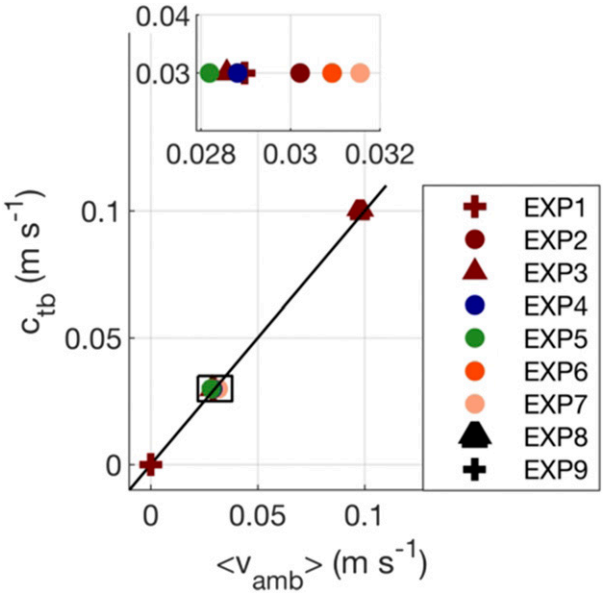

FIG. 14. The propagation speed of the transient bulge eddy compared to the tidally averaged alongshore velocities in the ambient ocean outside of the plume. The black line is a slope of 1, for comparison. The black box outlines the range shown in the zoomed-in insert shown above.

The coastal ocean circulation is relatively uniform offshore of the plume where there is no stratification or alongshore variability. When downwelling-favorable wind velocities of 2 and 4 m s^{-1} are imposed, alongshore tidally and depth-averaged velocities v_{amb} are 0.03 and 0.1 m s^{-1}, respectively (Fig. 14). That the unforced bulge eddy (in the absence of the ambient alongshore current induced by the wind forcing) does not propagate is consistent with the analytical and laboratory results from Nof (1988) and modeling study by Yankovsky et al. (2001). Due to the slow advection rate, freshwater volume within the bulge is transported relatively small distances alongshore (around 10–20 km over the first week after the pulse).

Following the passage of the nose, alongshore velocities and freshwater transport in the plume remain elevated until either the transient bulge eddy passes a given location or is no longer distinguishable relative to background conditions (e.g., Fig. 6). The time scale $\tau_{y=40}$ is shorter with stronger downwelling-favorable winds, smaller background discharge, a smaller pulse amplitude, and a shorter pulse duration, meaning that plume downstream of the transient bulge returns to background conditions more rapidly following the discharge pulse (Table 1).

f. Evolution of the plume in the case without winds

The plume response to the discharge pulse without downwelling-favorable winds (EXP9) deviates from the patterns observed in all of the other test cases explored here. Prior to the discharge pulse in EXP9 the net alongshore transport for $y \geq 2$ km is less than Q_B (Fig. 15a) because freshwater is accumulating within the bulge. As in the pulsed experiments with steady downwelling-favorable winds, there is a peak in $\langle Q_{FW,31.9} \rangle$ that propagates downstream following the pulse (white line), but it is indistinguishable from background variability beyond $y \simeq 60$ km, and the peak magnitude decreases as it propagates. There is only a single local peak in $\langle Q_{FW,31.9} \rangle$ near the river mouth and no secondary peak associated with a transient bulge eddy (as in Fig. 6a). In examining the surface salinity and velocity, it is apparent that the bulge does not propagate alongshore, but remains near the river mouth and continues to grow over time (Figs. 15b, 16). The freshwater volume transported by the nose of the pulse at $y = 40$ km is <20% of V_P, indicating that most of the freshwater volume associated with the discharge pulse initially accumulates in the bulge (Table 1). From $t > 5$ days after the pulse, $\langle Q_{FW,31.9} \rangle$ beyond $y = 40$ km remains less than Q_B (e.g., Fig. 8b) and each tidal cycle, the freshwater volume contained within the plume between the river mouth and $y = 40$ km increases by 40%–50% of Q_B. The area $\langle A_{31.9} \rangle$ increases over time near the river mouth as well as along the coast (Fig. 15b), while $\langle v_{31.9} \rangle$ and $\langle F_{FW,31.9} \rangle$ decrease (Figs. 15c,d). The plume does not reach a tidally averaged steady-state condition.

4. Discussion

As it propagates downstream, the nose of the elevated discharge pulse can be identified by a fit to a sine function [Eq. (5)], based on the imposed discharge at the head of the river. Freshwater transport behind the nose can be described by an exponential decay [Eq. (7)]. This applies within the estuary and along the coast with steady downwelling-favorable winds and under no-wind conditions. However, this idealized study does not explore the role of estuarine processes or the bulge retention under more realistic conditions such as with time-varying winds. Additionally, the elevated propagation speed of the nose near the river mouth ($y \leq 70$ km) where ageostrophic, nonlinear dynamics can be important is not well described by steady, linear theory. Here we discuss some implications of these results for real-world applications as well as the application of linear theory to interpret the dependence of the alongshore propagation speed of the nose on the pulse characteristics and wind speed.

The ability to describe the nose by the sine function matching the pulse at the head of the river is consistent with observed correlations between coastal current velocities and river discharge (Münchow and Garvine 1993;

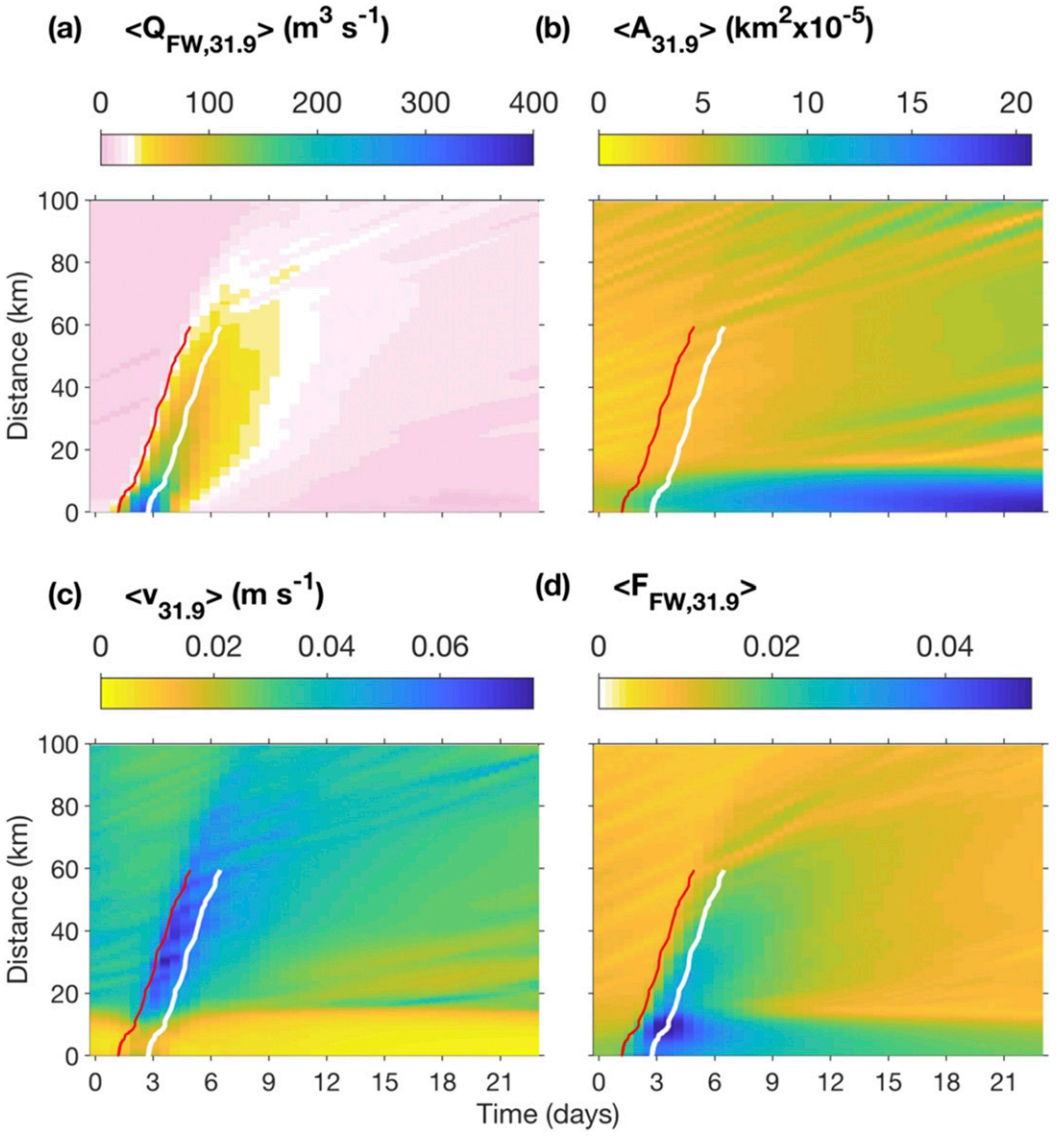

FIG. 15. (a) The tidally averaged freshwater transport within the 31.9-psu isohaline $\langle Q_{\mathrm{FW},31.9}\rangle$, (b) $\langle A_{\mathrm{FW},31.9}\rangle$, (c) $\langle v_{31.9}\rangle$, and (d) $\langle F_{\mathrm{FW},31.9}\rangle$ for EXP9 at cross sections alongshore following the pulse are plotted in color. The red line marks the time when $\langle Q_{\mathrm{FW},31.9}\rangle$ past each downstream location has first increased above Q_B and the white line traces the peak in $\langle Q_{\mathrm{FW},31.9}\rangle$ at t_n at each location alongshore.

Geyer et al. 2004; Mazzini et al. 2014). The sinusoidal shape and period of the freshwater transport signal is retained as the pulse propagates alongshore. Here it is shown that a high correlation between the velocity and freshwater transport in the river and far along the coast can exist even as the magnitude is decreased by both bulge and estuarine processes.

Estuarine mixing and adjustment impact the coastal plume. The far-field nose propagation speed is correlated with the density anomaly (Fig. 13d), indicating that mixing in the estuary may be important to the alongshore propagation speed even far from the river mouth. Additionally, estuarine adjustment likely contributes to a slight reduction in the pulse discharge V_n at the mouth relative to V_P at the head of the estuary. Although this impact is small (5%–11%) relative to reduction in the bulge (34%–87%), here only a simple river geometry is used, there is no spring–neap tidal variability, and the discharge and wind forcing are steady prior to the pulse so that the conditions within the estuary are greatly simplified. A detailed examination of how estuarine adjustment might impact the nose of the pulse following an event of elevated discharge under more realistic conditions is beyond the scope of this study.

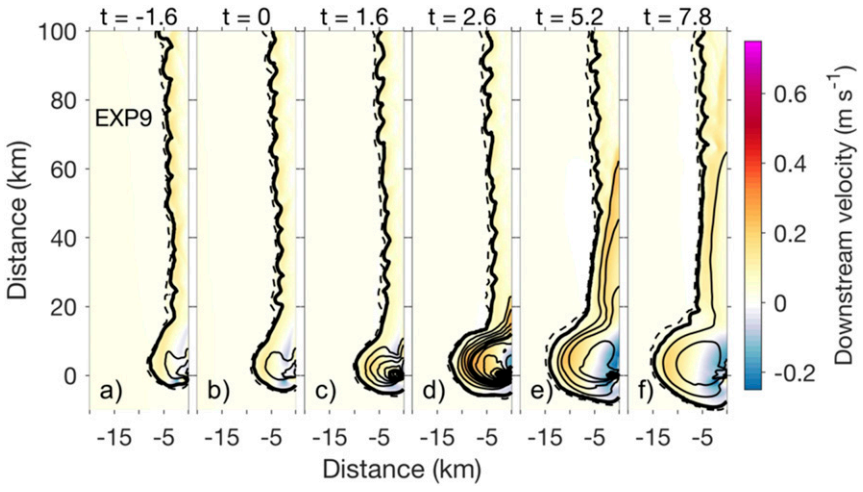

FIG. 16. Tidally averaged salinity and velocity profiles of the plume from EXP9 without wind forcing. Alongshore velocities are shown in color overlaid by salinity contours. The outermost thick contour demarcates the 31.9-psu isohaline with thick and thin contour lines at 5- and 1-psu intervals, respectively. The thin dashed line is at 31.99 psu.

The propagation speed of the nose c_n is fast and increases with pulse volume. Near the river mouth and in the region characterized by bulge dynamics and geostrophic adjustment of the plume, c_n is variable and not well described by the linear theory for the propagation speed of a buoyant coastal current from Lentz and Helfrich (2002) and Lentz and Largier (2006) (Figs. 12a,c). However, away from the river mouth, c_n is correlated with the plume freshwater fraction $\langle F_{\mathrm{FW},31.9}\rangle(t_n)$ and the downwelling-favorable wind speed, as predicted by this simplified geostrophic theory. Although the two-layer theory does not account for shear and stratification within the plume, it predicts the plume-averaged velocity in the nose $\langle v_{31.9}\rangle(t_n)$. The deviation between $\langle v_{31.9}\rangle(t_n)$ and c_n, which are equivalent in the steady, two-layer, alongshore-uniform theory for a coastal current, is likely due to the shear and stratification within the plume boundary. A more detailed understanding of the dynamics that control c_n are beyond the scope of this study. Here, we have demonstrated that this propagation speed can be fast (greater than or equal to the propagation speed c_s of a coastal current with a steady discharge equal to the peak pulse discharge Q_P), which can lead to the transport of discharge associated with the pulse relatively long distances alongshore.

The relatively strong dependence of $\tau_{y=40}$ on wind speed (it is smallest with high winds, and effectively infinite with no wind) motivates consideration of how the alongshore freshwater transport might respond to variations in wind speed. Although the winds are predominantly downwelling-favorable in the winter season, the alongshore wind speed varies on synoptic time scales (Fig. 1a). Previous observations and models have shown plumes to respond to local wind forcing on short time scales of roughly 3–6 h (e.g., Münchow and Garvine 1993; Hickey et al. 1998; García Berdeal et al. 2002). Oscillations in wind speeds during discharge events could further increase variability in alongshore freshwater transport as the bulge alternately accumulates and yields freshwater volume. Investigating the impact of wind variability on freshwater transport during pulsed discharge events, and the impact of the phasing of these processes, could be an important next step toward understanding buoyant plume dynamics in more realistic conditions.

These results have implications for the transport of waterborne materials that are exported to the coastal ocean during wintertime storm events. The relatively fast alongshore propagation of a significant fraction, $\mathcal{O}(50\%)$, of the freshwater volume associated with the pulse indicates that over the short time scales associated with these events, nutrients or carbon could potentially be transported tens of kilometers or more alongshore. The slower time scales associated with shedding of freshwater initially accumulated in the bulge and the alongshore propagation of the bulge indicate that waterborne materials may also have long residence times near the river mouth. These distributions primarily depend on pulse duration and wind speed, while the alongshore propagation speeds depend on pulse amplitude and duration as well as wind speeds.

5. Conclusions

A suite of simulations in an idealized coastal ocean domain using ROMS with varying steady background

discharge conditions (25–100 $m^3 s^{-1}$), pulse amplitude (200–800 $m^3 s^{-1}$), pulse duration (1–6 days), and steady downwelling-favorable winds (0–4 $m s^{-1}$) were compared to investigate the downstream freshwater transport along the coast following a discharge pulse from the river. For all of the pulsed discharge experiments with winds (EXP1–8), the evolution of the plume is qualitatively the same. From the initialization of the high discharge pulse through the return to steady-state conditions, the downstream freshwater transport past any cross section of the plume can be described by the superposition of the background discharge, the rapid passage of the pulse nose, and a slower exponential return to background values. While the pulse nose maintains the sinusoidal shape of the pulse forced at the head of the river, the amplitude is decreased by the estuary mouth and further decreased by the time it passes the bulge, resulting in a residual tail of elevated freshwater transport behind the nose. This response at the estuary mouth suggests that estuarine adjustment modifies the pulse. Following the pulse, the bulge grows and accumulates freshwater volume. The percentage of the pulse discharge initially retained near the river mouth (34%–87%) depends strongly on wind speed and pulse duration; for runs with the same wind speed (2 $m s^{-1}$) the dependence on pulse duration is consistent with the angle of incidence theory proposed by Yuan et al. (2018). The nose propagates quickly alongshore (at a rate of 0.04–0.32 $m s^{-1}$) associated with greater area-averaged freshwater fraction and alongshore velocities that remain relatively constant alongshore outside of the bulge. The alongshore propagation speed of the nose is strongly dependent on peak discharge, pulse duration, and wind speed. The transient bulge eddy moves more slowly downstream (at 0–0.1 $m s^{-1}$) and the freshwater volume initially accumulated within the bulge is shed into the plume farther downstream at an exponential rate (with an exponential time scale of 1.2–7.8 days). The bulge eddy propagation speed and exponential decay time scale are faster with stronger downwelling-favorable winds. As both the pulse characteristics and wind speeds impact the amount and length of time that freshwater volume can be retained near the river mouth, as well as the rate of alongshore freshwater transport in the nose, we recommend future investigation into the impact of time variability in discharge and wind forcing as well as the phasing of winds with discharge.

Acknowledgments. The authors are grateful to R. Matano, A. Kirincich, S. Lentz, and the anonymous reviewers for helpful comments and suggestions. Support for this research was provided by National Science Foundation Grants OCE1131238, OCE1260394, and OCE1829979.

REFERENCES

Avicola, G., and P. Huq, 2003: The role of outflow geometry in the formation of the recirculating bulge region in coastal buoyant outflows. *J. Mar. Res.*, **61**, 411–434, https://doi.org/10.1357/002224003322384870.

Barth, J. A., and P. A. Wheeler, 2005: Introduction to special section: Coastal advances in shelf transport. *J. Geophys. Res.*, **110**, C10S01, https://doi.org/10.1029/2005JC003124.

Brown, C., and R. Ozretich, 2009: Coupling between the coastal ocean and Yaquina Bay, Oregon: Importance of oceanic inputs relative to other nitrogen sources. *Estuaries Coasts*, **32**, 219–237, https://doi.org/10.1007/s12237-008-9128-6.

Burt, W. V., and W. B. McAlister, 1958: Hydrography of Oregon Estuaries: June 1956 to September 1959. Tech. Rep. Office of Naval Research 58-6, 17 pp.

Chant, R. J., and Coauthors, 2008: Dispersal of the Hudson River plume in the New York bight synthesis of observational and numerical studies during LaTTE. *Oceanography*, **21**, 148–161, https://doi.org/10.5670/oceanog.2008.11.

Chapman, D., 1985: Numerical treatment of cross-shelf open boundaries in a barotropic coastal ocean model. *J. Phys. Oceanogr.*, **15**, 1060–1075, https://doi.org/10.1175/1520-0485(1985)015<1060:NTOCSO>2.0.CO;2.

Chen, S.-N., 2014: Enhancement of alongshore freshwater transport in surface-advected river plumes by tides. *J. Phys. Oceanogr.*, **44**, 2951–2971, https://doi.org/10.1175/JPO-D-14-0008.1.

Choi, B.-J., and J. L. Wilkin, 2007: The effect of wind on the dispersal of the Hudson River plume. *J. Phys. Oceanogr.*, **37**, 1878–1897, https://doi.org/10.1175/JPO3081.1.

Flather, R. A., 1976: A tidal model of the northwest European continental shelf. *Mem. Soc. Roy. Sci. Liege*, **6**, 141–164.

Fong, D. A., and W. R. Geyer, 2002: The alongshore transport of freshwater in a surface-trapped river plume. *J. Phys. Oceanogr.*, **32**, 957–972, https://doi.org/10.1175/1520-0485(2002)032<0957:TATOFI>2.0.CO;2.

Galperin, B., L. H. Kantha, S. Hassid, and A. Rosati, 1988: A quasi-equilibrium turbulent energy model for geophysical flows. *J. Atmos. Sci.*, **45**, 55–62, https://doi.org/10.1175/1520-0469(1988)045<0055:AQETEM>2.0.CO;2.

García Berdeal, I., B. M. Hickey, and M. Kawase, 2002: Influence of wind stress and ambient flow on a high discharge river plume. *J. Geophys. Res.*, **107**, 3130, https://doi.org/10.1029/2001JC000932.

Garvine, R. W., 1995: A dynamical system for classifying buoyant coastal discharges. *Cont. Shelf Res.*, **15**, 1585–1596, https://doi.org/10.1016/0278-4343(94)00065-U.

Geyer, W. R., R. P. Signell, D. A. Fong, J. Wang, D. M. Anderson, and B. A. Keafer, 2004: The freshwater transport and dynamics of the western Maine coastal current. *Cont. Shelf Res.*, **24**, 1339–1357, https://doi.org/10.1016/j.csr.2004.04.001.

Haidvogel, D. B., H. G. Arango, K. Hedstrom, A. Beckmann, P. Malanotte-Rizzoli, and A. F. Shchepetkin, 2000: Model evaluation experiments in the North Atlantic Basin: Simulations in nonlinear terrain-following coordinates. *Dyn. Atmos. Oceans*, **32**, 239–281, https://doi.org/10.1016/S0377-0265(00)00049-X.

Hetland, R. D., 2005: Relating river plume structure to vertical mixing. *J. Phys. Oceanogr.*, **35**, 1667–1688, https://doi.org/10.1175/JPO2774.1.

——, and W. R. Geyer, 2004: An idealized study of the structure of long, partially mixed estuaries. *J. Phys. Oceanogr.*, **34**, 2677–2691, https://doi.org/10.1175/JPO2646.1.

Hickey, B. M., and N. S. Banas, 2003: Oceanography of the U.S. Pacific Northwest coastal ocean and estuaries with application

to coastal ecology. *Estuaries*, **26**, 1010–1031, https://doi.org/10.1007/BF02803360.

——, L. J. Pietrafesa, D. A. Jay, and W. C. Boicourt, 1998: The Columbia River plume study: Subtidal variability in the velocity and salinity fields. *J. Geophys. Res.*, **103**, 10 339–10 368, https://doi.org/10.1029/97JC03290.

Horner-Devine, A. R., 2009: The bulge circulation in the Columbia River plume. *Cont. Shelf Res.*, **29**, 234–251, https://doi.org/10.1016/j.csr.2007.12.012.

——, D. A. Jay, P. M. Orton, and E. Y. Spahn, 2009: A conceptual model of the strongly tidal Columbia River plume. *J. Mar. Syst.*, **78**, 460–475, https://doi.org/10.1016/j.jmarsys.2008.11.025.

——, R. D. Hetland, and D. G. MacDonald, 2015: Mixing and transport in coastal river plumes. *Annu. Rev. Fluid Mech.*, **47**, 569–594, https://doi.org/10.1146/annurev-fluid-010313-141408.

Hunter, E. J., R. J. Chant, J. L. Wilkin, and J. Kohut, 2010: High-frequency forcing and subtidal response of the Hudson River plume. *J. Geophys. Res.*, **115**, C07012, https://doi.org/10.1029/2009JC005620.

Huyer, A., 1977: Seasonal-variation in temperature, salinity, and density over continental-shelf off Oregon. *Limnol. Oceanogr.*, **22**, 442–453, https://doi.org/10.4319/lo.1977.22.3.0442.

——, E. Sobey, and R. Smith, 1979: Spring transition in currents over the Oregon continental-shelf. *J. Geophys. Res.*, **84**, 6995–7011, https://doi.org/10.1029/JC084iC11p06995.

Kilcher, L. F., J. D. Nash, and J. N. Moum, 2012: The role of turbulence stress divergence in decelerating a river plume. *J. Geophys. Res.*, **117**, C05032, https://doi.org/10.1029/2011JC007398.

Lentz, S. J., and K. R. Helfrich, 2002: Buoyant gravity currents along a sloping bottom in a rotating fluid. *J. Fluid Mech.*, **464**, 251–278, https://doi.org/10.1017/S0022112002008868.

——, and J. Largier, 2006: The influence of wind forcing on the Chesapeake Bay buoyant coastal current. *J. Phys. Oceanogr.*, **36**, 1305–1316, https://doi.org/10.1175/JPO2909.1.

Lerczak, J., W. Geyer, and D. Ralston, 2009: The temporal response of the length of a partially stratified estuary to changes in river flow and tidal amplitude. *J. Phys. Oceanogr.*, **39**, 915–933, https://doi.org/10.1175/2008JPO3933.1.

MacDonald, D. G., and W. R. Geyer, 2004: Turbulent energy production and entrainment at a highly stratified estuarine front. *J. Geophys. Res.*, **109**, C05004, https://doi.org/10.1029/2003JC002094.

Marchesiello, P., J. C. McWilliams, and A. Shchepetkin, 2001: Open boundary conditions for long-term integration of regional oceanic models. *Ocean Modell.*, **3**, 1–20, https://doi.org/10.1016/S1463-5003(00)00013-5.

Mazzini, P. L. F., J. A. Barth, R. K. Shearman, and A. Erofeev, 2014: Buoyancy-driven coastal currents off Oregon during fall and winter. *J. Phys. Oceanogr.*, **44**, 2854–2876, https://doi.org/10.1175/JPO-D-14-0012.1.

McCabe, R. M., B. M. Hickey, and P. MacCready, 2008: Observational estimates of entrainment and vertical salt flux in the interior of a spreading river plume. *J. Geophys. Res.*, **113**, C08027, https://doi.org/10.1029/2007JC004361.

Milliman, J., and J. Syvitski, 1992: Geomorphic tectonic control of sediment discharge to the ocean: The importance of small mountainous rivers. *J. Geol.*, **100**, 525–544, https://doi.org/10.1086/629606.

Mork, M., 1981: Circulation phenomena and frontal dynamics of the Norwegian coastal current. *Philos. Trans. Roy. Soc. London*, **302A**, 635–647, https://doi.org/10.1098/rsta.1981.0188.

Münchow, A., and R. Garvine, 1993: Dynamical properties of a buoyancy-driven coastal current. *J. Geophys. Res.*, **98**, 20 063–20 077, https://doi.org/10.1029/93JC02112.

Nof, D., 1988: Eddy-wall interactions. *J. Mar. Res.*, **46**, 527–555, https://doi.org/10.1357/002224088785113540.

——, and T. Pichevin, 2001: The ballooning of outflows. *J. Phys. Oceanogr.*, **31**, 3045–3058, https://doi.org/10.1175/1520-0485(2001)031<3045:TBOO>2.0.CO;2.

Orlanski, I., 1976: A simple boundary condition for unbounded hyperbolic flows. *J. Comput. Phys.*, **21**, 251–269, https://doi.org/10.1016/0021-9991(76)90023-1.

Royer, T., 1981: Baroclinic transport in the Gulf of Alaska. Part II A fresh-water driven coastal current. *J. Mar. Res.*, **39**, 251–266.

Shchepetkin, A. F., and J. C. McWilliams, 1998: Quasi-monotone advection schemes based on explicit locally adaptive dissipation. *Mon. Wea. Rev.*, **126**, 1541–1580, https://doi.org/10.1175/1520-0493(1998)126<1541:QMASBO>2.0.CO;2.

——, and ——, 2005: The Regional Oceanic Modeling System (ROMS): A split-explicit, free-surface, topography-following-coordinate oceanic model. *Ocean Modell.*, **9**, 347–404, https://doi.org/10.1016/j.ocemod.2004.08.002.

Sigleo, A. C., and W. E. Frick, 2007: Seasonal variations in river discharge and nutrient export to a northeastern Pacific estuary. *Estuarine Coastal Shelf Sci.*, **73**, 368–378, https://doi.org/10.1016/j.ecss.2007.01.015.

Smolarkiewicz, P., and T. Clark, 1986: The multidimensional positive definite advection transport algorithm: Further development and applications. *J. Comput. Phys.*, **67**, 396–438, https://doi.org/10.1016/0021-9991(86)90270-6.

Umlauf, L., and H. Burchard, 2003: A generic length-scale equation for geophysical turbulence models. *J. Mar. Res.*, **61**, 235–265, https://doi.org/10.1357/002224003322005087.

Vörösmarty, C. J., B. M. Fekete, M. Meybeck, and R. B. Lammers, 2000: Global system of rivers: Its role in organizing continental land mass and defining land-to-ocean linkages. *Global Biogeochem. Cycles*, **14**, 599–621, https://doi.org/10.1029/1999GB900092.

Wheatcroft, R. A., M. A. Goni, J. A. Hatten, G. B. Pasternack, and J. A. Warrick, 2010: The role of effective discharge in the ocean delivery of particulate organic carbon by small, mountainous river systems. *Limnol. Oceanogr.*, **55**, 161–171, https://doi.org/10.4319/lo.2010.55.1.0161.

Whitehead, J. A., 1985: The deflection of a baroclinic jet by a wall in a rotating fluid. *J. Fluid Mech.*, **157**, 79–93, https://doi.org/10.1017/S0022112085002312.

Yankovsky, A. E., and D. C. Chapman, 1997: A simple theory for the fate of buoyant coastal discharges. *J. Phys. Oceanogr.*, **27**, 1386–1401, https://doi.org/10.1175/1520-0485(1997)027<1386:ASTFTF>2.0.CO;2.

——, B. M. Hickey, and A. K. Munchow, 2001: Impact of variable inflow on the dynamics of a coastal buoyant plume. *J. Geophys. Res.*, **106**, 19 809–19 824, https://doi.org/10.1029/2001JC000792.

Yuan, Y., A. R. Horner-Devine, M. Avener, and S. Bevan, 2018: The role of periodically varying discharge on river plume structure and transport. *Cont. Shelf Res.*, **158**, 15–25, https://doi.org/10.1016/j.csr.2018.02.009.

Zeng, X., Q. Zhang, D. Johnson, and W.-K. Tao, 2002: Parameterization of wind gustiness for the computation of ocean surface fluxes at different spatial scales. *Mon. Wea. Rev.*, **130**, 2125–2133, https://doi.org/10.1175/1520-0493(2002)130<2125:POWGFT>2.0.CO;2.